Electrical Characterisation of ZnO and ZnO Schottky barrier diodes

by

Meehleketo Advice Mayimele

University of Pretoria

Submitted in partial fulfilment of the requirements of the degree

Magister Scientiae

in the

Faculty of Natural and Agricultural Science at the University of Pretoria

Promoter: **Prof. M. Diale**

Co-Promoter: **Prof. F. D. Auret**

February 2016

Electrical characterization of ZnO and ZnO Schottky barrier diodes

by

Meehleketo Advice Mayimele

Submitted in partial fulfilment of the requirements of the degree

MSc (Physics)

in the

Faculty of Natural and Agricultural Science

University of Pretoria

Promoter: **Prof. M Diale**

Co-Promoter: **Prof. F.D Auret**

The electrical properties of ZnO and Schottky contacts to ZnO have been investigated using different techniques. Good rectifying Schottky contact has been fabricated on ZnO, after treating the samples with boiling hydrogen peroxide. Electrical properties of these Schottky contacts have been investigated using current-voltage (*IV*) and capacitance-voltage (*CV*) measurements in the temperature range (20-350 K). Schottky barrier heights (SBHs) determined using temperature-dependent *IV* measurements have been observed to increase with temperature and this has been explained as an effect of the barrier inhomogeities. The Schottky contacts have indicated the dominance of predominantly thermionic emission at room temperature and the existence of other current transport mechanisms at lower temperatures.

Palladium Schottky barrier diodes on melt grown n-ZnO were irradiated with alpha-particles from a Van de Graaff accelerator. To determine the effect of these changes on the electrical characteristics of Schottky contacts several techniques were used. The *CV* measurements showed a decrease in the free carrier concentration with increase in fluence. Deep level transient spectroscopy (DLTS) was used to determine the concentrations, capture cross-sections, introduction rate and energy level in the bandgap of deep level defects introduced during the alpha-particles irradiation.

Declaration

I Meehleketo Advice Mayimele declare that the dissertation, which I hereby submit for the degree Masters of Science (MSc) in Physics at the University of Pretoria, is my own work and has not previously been submitted by me for a degree at this or any other tertiary institution.

Signature…….. Date …./…./201...

To My mother

Nxalati Baby Baloyi

Aunt

Staff Gavaza Baloyi-Zitha

Failure is a test of how strong you are

and

how much do you want something….

My Sons and Friends

Mafemani **&** **Samuel** **Mayimele**

Acknowledgements

For the success of this study, I cannot fully thank the people who made it possible

- My supervisor Professor M Diale and Co-Supervisor Professor F.D Auret for support, guidance and discussions throughout my MSc study.
- My mentor Dr W. Mtangi for guidance and discussions during the course of this work.
- Johan Janse Van Rensburg for all the assistance with the measuring equipment and discussions in the laboratory.
- I would also like to extend many thanks the following members of the Electronic material and Thin Films Group whose contribution is appreciated; Prof W. E. Meyer, Dr S.M.M Coelho, M.J. Legodi, L. van Schalkwyk, Dr C. Zander, P.M.N. Ngoepe, H.T. Danga, E. Omotoso, F. J. Nambala, S.M Tunhuma, K Maabong, A.T Paradzah and K. Ostvar.
- I want to thank the Head of the Physics Department, Prof Chris Theron for affording me an opportunity to do part time work in the department.
- I would like to thank my friends: Nhluvuko, Brain, Tiyisalani, Xikombiso, Ednah,Tervin, Ireland, Malifu, Chris, Joeman, Jabu, Dakalo, Smile, Didi, Dumisani, Dr Mkapu, Gay, Nyiko, Lassy, Rhulani, Mike, Comment, Andrew, Nhlamulo, Rise, Evah, Sammy, Mandla, Reen, Rusty, Condry, Jennifer, Matshidiso, Rivalani, Miyelani, Mapapila, Tshepo, Mpho, Vunene, Manzine, Peace, Magazi, Tiyani, Kevin, Weaven, Dede, Ocanto Latino Boys and all who always believed in me.
- Special thanks to my sister Nhluvuko G-nine Mayimele.
- Lastly, I want to thank my family for their love, support and always believing in me.

Above everything else, I thank the Lord; God in heaven whom I believe makes all things possible.

Table of Contents

Chapter 1

Introduction

ZnO is a well-known II-IV semiconductor with a direct wide bandgap of 3.37 eV and a large excitonic binding energy of 60 meV at room temperature [1]. The direct wide bandgap of the ZnO enables the semiconductor to be a good candidate for optoelectronic applications and the large exciton energy helps to employ the excitonic recombination process as a lasing mechanism [2]. ZnO exists mostly as n-type, whose conductivity is supposedly due to the existence of native point defects, such as O vacancies and Zn interstitials [3]. Some other impurities, such as Al, Mg, H, are also claimed to contribute to the n-type conductivity in ZnO [4]. Many wide bandgap semiconductors exists as doping asymmetry i.e., easy to get n-type ZnO, but rather difficult to produce p-type ZnO [3].

ZnO is a polar semiconductor material with two crystallographic planes that have opposite polarity and different relaxation energies, which lead to a higher growth rate along the c-axis i.e., the formation of nanorods-like vertical structures [2]. ZnO exists in zincblende, cubic rocksalt and wurtzite crystal structures: however, at ambient temperature and pressure, ZnO crystallizes normally in a wurtzite structure with a hexagonal lattice that has two interconnecting sub-lattices of Zn^{2+} and O^{2-} with the Zn ion surrounded by tetrahedral O ions and vice versa [5, 6]. This tetrahedral coordination gives rise to a polar symmetry along the hexagonal axis, which is responsible for a number of the chemical and physical properties of ZnO, including the piezoelectricity and spontaneous polarization [7]. The structure of ZnO is a key factor in crystal growth, etching and defect generation.

From a technological point of view, ZnO is an essential, multi-functional material with a number of applications in biosensors, chemical sensors, gas sensors, dye-sensitized solar cells, electronics, piezoelectric devices, smart windows, UV-lasers, UV-photodetectors [5, 8]. In addition, the ferromagnetic properties of rare-earth metals doped ZnO show potential for spintronic based devices. Further, ZnO is a biocompatible material with antibacterial and other novel properties, which enables it to be utilized in a variety of applications, such as drug delivery, medical products, bio-imaging, cancer treatment, sunscreens, skin lotions etc. [6, 9]. ZnO films can be produced by methods amenable to large-scale manufacturing at temperatures that allow for low cost operation and flexible substrates. Finally, thin films of ZnO offer the advantage of monolithic integration with advanced complementary metal-

oxide-semiconductor (CMOS) technology for highly sensitive and selective chemical and/or biological sensors arrays [2].

Apart from native point defects, ZnO also possesses deep level emission bands that emit all colours in the visible range with good colour rendering properties [8]. A good understanding of the defect identity, defect control, properties and influence on devices [10, 11] and control of defects is essential to improve efficiency of devices. In addition, an understanding of the origins of emissions related to deep level defects in ZnO for development of highly efficient optoelectronic devices is required, i.e. to introduce them if necessary. Annealing of crystals is one possible way of recovering or removing defects in semiconductors. Defects can also be intentionally introduction in semiconductor material by irradiating with energetic particles [12].

Defect characterization in semiconductors is essential for the fabrication of high quality devices. Different techniques have been used to characterize defects in semiconductors, some of which include the X-ray diffraction, admittance spectroscopy, cathodoluminescence, and photoluminescence, Rutherford backscattering spectroscopy, position annihilation spectroscopy and Hall measurements. In this dissertation, deep level transient spectroscopy (DLTS) has been used to characterize deep level defects in ZnO. The DLTS is a capacitance based spectroscopy technique that gives information about the signature of an electrically active state, i.e. the activation enthalpy and capture cross-section within the bandgap of the semiconductor [13].

The fabrication of high quality devices also requires a good understanding of current transport mechanisms in a metal-semiconductor contact [14]. It has been report that analysis of the electrical characteristics of the Schottky barrier diodes (SBDs) only at room temperature does not give sufficient information about the conduction process [15, 16]. Since current transport mechanisms vary with different temperature ranges, there is a need to conduct temperature dependent current-voltage measurements to comprehensively describe the current transport mechanism and determine accurate values of the diode parameters at different temperatures.

An overview of ZnO semiconductor properties is presented in chapter 2. Chapter 3 contains the metal-semiconductor contacts. The electrical characterization techniques are given in chapter 4. Experimental techniques performed in this particular work are outlined in chapter

5. Chapter 6 gives an outline of the results and discussion obtained from this work. A summary of conclusions drawn from this study are presented in chapter 7.

Chapter 2

ZnO semiconductor properties

2.1 Introduction

ZnO has been widely studied since 1935 and in the last few decades has attracted much attention from the research community. This is due to its wide and direct band gap, large exciton binding energy, high electron mobility, high thermal conductivity, low power threshold for optical pumping, radiation hardness and biocompatibility [1, 5, 17]. In addition, its broad chemistry leads to many opportunities for wet chemical etching [18, 19]. These properties make ZnO an ideal candidate for a variety of devices ranging from ultraviolet to blue range optoelectronics, transparent thin-film transistors, field effect transistors, spintronics, photodetectors, lasers, sensors, microwave diodes and light emitting diodes [20]. In this chapter, semiconductor theoretical aspects are discussed. In section 2.2 and 2.3 presents, the crystal and energy band structures respectively, for ZnO. The growth techniques are discussed in section 2.4. Section 2.5 and 2.6 the fundamentals of defects in semiconductors and the properties and device applications are presented respectively.

2.2 Crystal Structure

ZnO occurs as an identical attachment of the basis atoms (Zn and O) to every lattice point, with three lattice structures: the scarcely observed cubic rocksalt, hexagonal wurtzite and zincblende. This tetrahedral coordination is a typical of sp^3 covalent bonding nature, but these materials also have a substantial ionic character that tend to increase the band gap beyond the one expected from covalent bonding [21]. The zincblende structures are grown on substrate with cubic lattice to produce a stable structure and the cubic rocksalt (NaCl) structure is most stable at relatively high pressures [5]. Meanwhile, the wurtzite structure is thermodynamically stable at ambient conditions. The wurtzite structure in Fig. 2.1 can be considered as two interpenetrating hexagonal-close-packed lattices, designated by two interconnecting sublattices of Zn^{2+} and O^{2-} such that each oxygen ion is surrounded by a tetrahedral of zinc ions and vice versa [8]. This tetrahedral coordination gives rise to a polar symmetry along the hexagonal axis, which is responsible for a number of the chemical and physical properties of ZnO, including the piezoelectricity and spontaneous polarization [5].

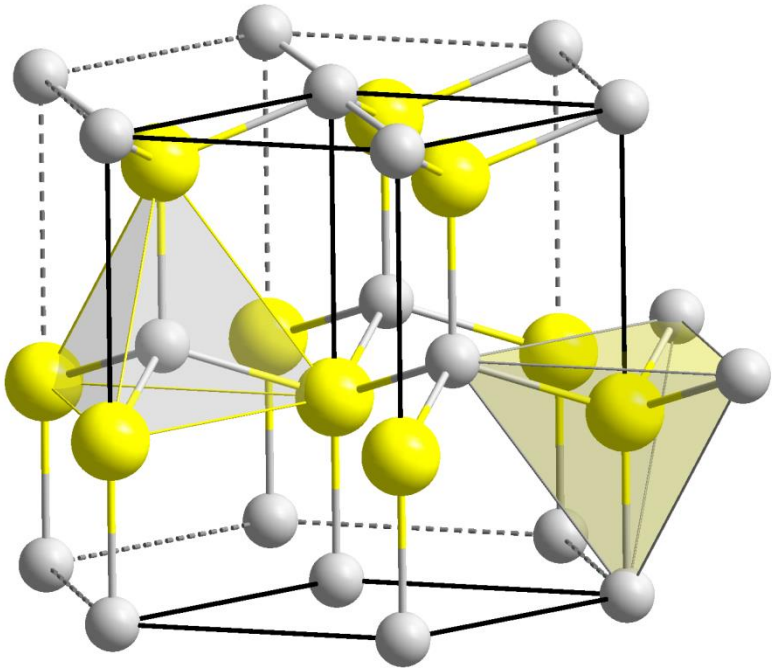

Fig. 2.1: The hexagonal wurtzite structure of ZnO, where Zn atoms shown as small white spheres and O atoms as large yellow spheres [8].

2.3 Band structure

In semiconductors, band structures can be used to determine the most important properties such as the band gap, effective electron and hole mass and the potential application of the material. There are numerous ways to calculate the electronic band structure of ZnO [8, 20, 22]. The local density approximation (LDA) and incorporating atomic self-interaction corrected pseudopotentials (Sic-PP) were used to calculate the band structure as presented in Fig. 2.2. The band structure of ZnO is calculated by taking the 3d electrons of Zn into consideration to accurately account for the trend shown in Fig. 2.2 [8]. In ZnO, the $4s$ and $4p$ orbitals are almost unoccupied instead the $3d$ orbital are occupied with Zn electrons when using the Sic-PP model. The 2s-orbitals and the 2p-orbitals are partially occupied by O electrons, with an average occupation of about 0.8. The theoretical calculations using the pseudo potential methods on the band structure of ZnO have a qualitative agreement with experimental observations [18].

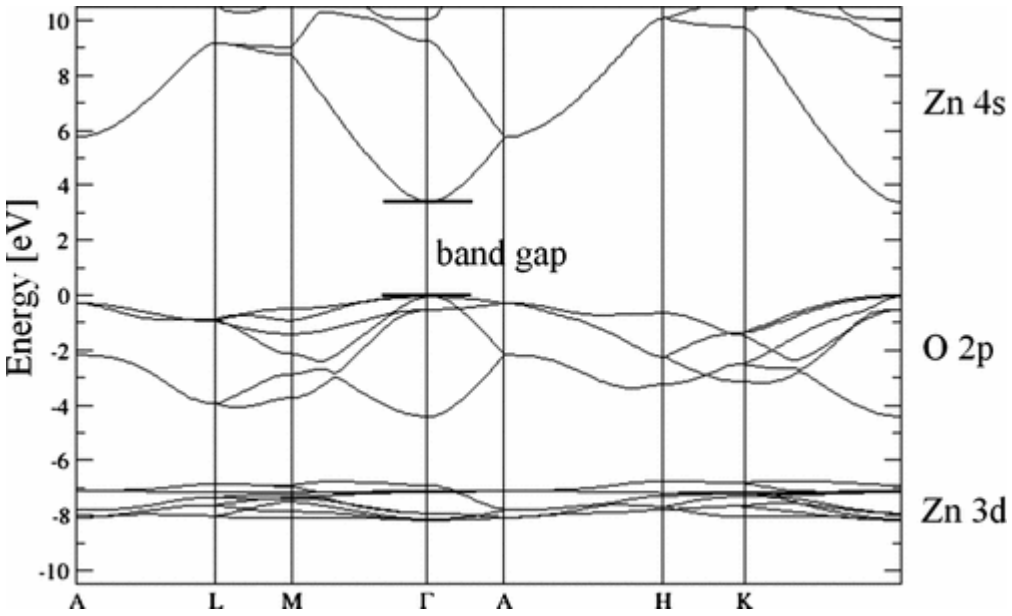

Fig. 2.2: Band structure of bulk ZnO (in the wurtzite structure) calculated with modified self-interaction corrected pseudopotential [8].

2.4 Growth techniques

The growth of ZnO thin films and bulk single crystals has being studied using different techniques which are identified below [5]. Thin films materials are grown using radio frequency (RF) magnetron sputtering [23], pulsed laser deposition (PLD) [24], molecular beam epitaxy (MBE) [25], metalorganic chemical vapour deposition (MOCVD) [26] and organometal vapour-phase epitaxy (OMVPE) [27]. These growth techniques gave way to advancement of biosensors due to their biocompatibility, chemical stability, high isoelectric point, electrochemical activity, high electron mobility, ease of synthesis by diverse methods and high surface-to-volume ratio [28].

Bulk crystals have received a vast interest in recent decades, due to its important properties in the design of electronic devices. Lately, significant developments were established on growth techniques in order to grow high quality crystals. Remarkable improvements were made in the growth of bulk crystals with regard to reproducibility, thermal stability, uniformity, impurity and dopant control. However, bulk materials are mainly grown by seeded chemical vapour transport (SCVT) [29], hydrothermal [30] and melt growth techniques [31]. In SCVT, growth of ZnO high quality single crystals were grown at lower temperatures in a quartz vessel and the nucleation process is better controlled. SCVT growth method downside is the low growth rate (∽0.08 mm/h). In the hydrothermal method, the growth takes place in a platinum-lined autoclave held at relatively low temperatures in the range 300–400 ◦C. ZnO is dissolved in a KOH/LiOH base solution in a high temperature and pressure region, and

precipitated in a region of reduced temperature. Hydrothermal growth has resulted in large ZnO crystals with high crystalline quality up to 2 inches in diameter, allowing the production of high-quality large substrates for homoepitaxy and heteroepitaxy. It is characterized by slow growth rates of about 0.03 inches per day and unavoidable incorporation of impurities coming from the solvent, such as Li and K, that may strongly affect the electrical properties of these type of samples [8, 32]. In this particular study, the main focus will be melt grown bulk ZnO single crystal manufactured by Cermet Inc. in Atlanta, Georgia. The melt growth technique has many advantages, such as a high growth rate (> 5 mm/h), high quality material that is free of solvent related impurities, and thus minimal defects. In addition, it has a high flexibility to grow in any crystal orientation and ease of doping the crystals to achieve the desired electronic characteristic.

2.5 Defects in ZnO

In real life situations, perfect crystals are difficult to obtain: these can be attributed to several factors including growth conditions and growth techniques. During crystal growth, intentionally, some impurities can be introduced into the material, thereby disturbing the orientation of the host atoms. Some defects in a material can be introduced or removed by post-growth annealing [7]. Defects in semiconductor materials can among others be associated to impurities, missing atoms, dopants and wrong position occupation of atoms which disturb the crystal structure [3].

The defects introduced in material may cause electronic states in the bandgap of semiconductor material. The electronic states introduced by these defects can be classified as shallow and deep levels depending on their location relative to the conduction or valence band edge. Shallow level defects have a transition level positioned in such a way that it can be thermally ionized at room temperature or the device operating temperature [33]. In ZnO, shallow level defects include group I related metals, which are located just a few tens of milli-electron volts (meV) below the bottom of the conduction band minimum [34]. Deep level defects which includes Zn and O vacancies are said to be located within the middle third of the semiconductor bandgap and at room temperature are usually unionized.

Defects in semiconductor material can be categorized into two sections, point defects and extended defects. Point defect constitutes a large concentration of defects in semiconductors and causes some perturbation of the lattice within a localized area about a lattice site involving only a few nearest neighbours [11]. The growth or annealing conditions determines the formation energy in point defects. Point defects are classified as intrinsic and extrinsic

lattice defects. Intrinsic lattice defects are those caused by missing host atoms (O/Zn vacancies), interstials and host atoms occupying wrong lattice site (antisites) [9]. Extrinsic lattice defects are due to impurity atoms occupying substitutional or interstitial sites [35]. In ZnO, the intrinsic lattice point defects of interest are vacancies and host interstitials associated with the two sublattices [8].

Point defects affecting ZnO can be controlled in many ways: by background doping, minority carrier lifetime and luminescence efficiency. Such defects can cause device degradation as they also assist the diffusion mechanisms that are involved during growth and processing of ZnO [35]. These pose a challenge in the growing of p-type ZnO. The high levels of unintentional n-type conductivity in ZnO can be attributed to the native point defects [8]. A good understanding of the nature and origins of these point defects in ZnO is essential. The native point defects in ZnO include O and Zn vacancy, O and Zn antisites, O and Zn interstitials [8, 36, 37]. Extrinsic point defects include hydrogen and other impurities introduced during growth [38].

On the other hand, extended defects in semiconductors are known as volume defects, surface defects and line defects. Volume defects are identified to be any volume that differs from the rest of the crystal in structure, orientation, composition and state variables [5, 38] i.e. precipitates, second phase grains and grains in polycrystalline materials. Surface defects are defined to be free of the surface or interface between distinguishable volumes. These are usually caused by the surface conduction in bulk ZnO material, with a free carrier concentration. The effects of surface conduction were observed from the Hall Effect measurements [39]. Line defects are classified into different categories, namely dislocations and disclinations. Disclinations are usually observed in liquid crystals in which the rotational symmetry of crystals is violated [6].

2.6 Properties and device applications

2.6.1 Basic properties of ZnO

Table 2.1 shows the basic properties of ZnO. It should be noted that there still exists uncertainty in some of these values. For example, there have few reports of p-type ZnO and therefore the hole mobility and effective mass are still in debate. Similarly, the values for thermal conductivity shows some spread in values and this may be a result of the influence of defects such as dislocations. The values of carrier mobility will undoubtedly increase as more control is gained over compensation and defects in the material [5].

Table 2.1: Properties of wurtzite ZnO [8]

Property	Value
Lattice parameters at 300 K: a_o c_o	 0.32495 nm 0.52069 nm
a_o/c_o	1.602 (ideal hexagonal structure shows 1.633)
u	0.345
density	5.606 g/cm^3
Melting point	1975 ^{o}C
Thermal conductivity	0.6, 1-1.2
Linear expansion coefficient (/^{o}C)	a_o : 6.5 × 10^{-6} , c_o : 3.0 × 10^{-6}
Static dielectric constant	8.656
Refractive index	2.008, 2.029
Energy gap	3.4 eV, direct
Intrinsic carrier concentration	<10^6 cm^{-3} (max n-type doping >10^{20} cm^{-3} electrons; max p-type doping <10^{17} cm^{-3} holes)
Exciton binding energy	60 meV
Electron effective mass	0.24
Electron Hall mobility at 300 K for n-type conductivity	200 cm^2/V s
Hole effective mass	0.59
Electron Hall mobility at 300 K for p-type conductivity	5-50 cm^2/V s

2.6.2 Optoelectric device applications

ZnO-based thin films and nanostructures have been used for various emerging applications such as gas sensors, surface acoustic wave devices and optoelectronic devices. Aluminium doped zinc oxides (AZO) thin films are currently displacing indium tin oxide (ITO) for transparent conducting oxides (TCO) applications due to recent improvements in attainable AZO conductivity combined with processing, cost and toxicity advantages. Advances in the channel mobilities and improvement of on/off ratios in ZnO-based transparent thin film transistors (TTFT) have opened up the potential for use as a replacement for Si in AM-OLED and AM-LCD screens [1]. Angular-dependent specular reflection measurements of self-forming, moth-eye like, nanostructure arrays grown by PLD were seen to have <0.5% reflectivity over the whole visible spectrum for angles of incidence between 10 and 60 degrees. Such nanostructures may be useful for applications such as anti-reflective coatings on solar cells. Compliant ZnO layers on mismatched/amorphous substrates were shown to have potential for MOVPE regrowth of GaN. This approach could be used as means to facilitate lift-off GaN-based solar cells on cheap substrates. The green gap in InGaN-based LEDs were combatted by substituting low temperatures PLD n-ZnO for MOCVD n-GaN inverted hybrid heterojunctions [22, 27].

2.6.3 Gas sensing

ZnO has a long history of use as a gas sensing material [1, 5]. There is a strong interest in the development of wide bandgap semiconductor gas sensors for applications including detection of combustion gases for fuel leak detection in spacecraft, automobiles and aircraft, fire detectors, exhaust diagnosis and emissions from industrial processes. Of particular interest are methods for detecting ethylene (C_2H_4), which offers problems because of its strong double bonds and hence the difficulty in dissociating it at modest temperatures. Wide bandgap semiconductors such as ZnO are capable of operating at much higher temperatures than more conventional semiconductors like Si and Ge. Diodes structures based on field-effect transistors are sensitive to gases such as hydrogen and hydrocarbons. Ideal gas sensors have the ability to discriminate between different gases and arrays that contain different metal oxides such as SnO_2, ZnO, CuO and WO_3 on the same chip can be used to detect different gases [7]. The gas sensing mechanism suggested include the desorption of adsorbed surface oxygen and grain boundaries in polycrystalline ZnO [3], exchange of charges between adsorbed gas species and the ZnO surface leading to changes in depletion depth and changes in surface or grain boundary conduction by gas adsorption/desorption [6, 7].

Chapter 3

Metal-Semiconductor Contacts

3.1 Introduction

Metal-semiconductor contacts are an important part of virtually all semiconductor electronic and optoelectronic devices. The study of metal semiconductor rectifying contact dates back to 1874, where Braun reported the dependence of the total resistance on the polarity of the applied voltage and on detailed surface conditions [26, 33]. Thus, paving a way to a theory that explains the transport of electrons over the potential barrier through drift and diffusion, attributed to Schottky and Mott in 1938 [40]. In this chapter, the theory of ideal metal-semiconductor contacts, the concept of the barrier height and different current conduction mechanisms are discussed.

3.1.1 Energy band

Consider a metal and a semiconductor brought into contact assuming no surface states, and they have different electronic configurations and band structures. The Fermi levels of the semiconductor and metal located at different energies within the energy bandgap were aligned in process known as band bending[41]. If a metal with a work function greater than that of semiconductor are brought into contact, electrons diffuse from high to low energy side, therefore lowering their energy. Thus, the excess negative charge build up in the metal will repel electrons flowing from the conduction band of the semiconductor to the metal. The high-energy electrons in the region adjacent to the metal would have moved into the metal, so the Fermi level in the semiconductor will align with that of the metal. The generated electric potential causes the deformation of the energy bands in the semiconductor near the metal-semiconductor interface, yielding a structure shown in Fig. 3.1 [42],

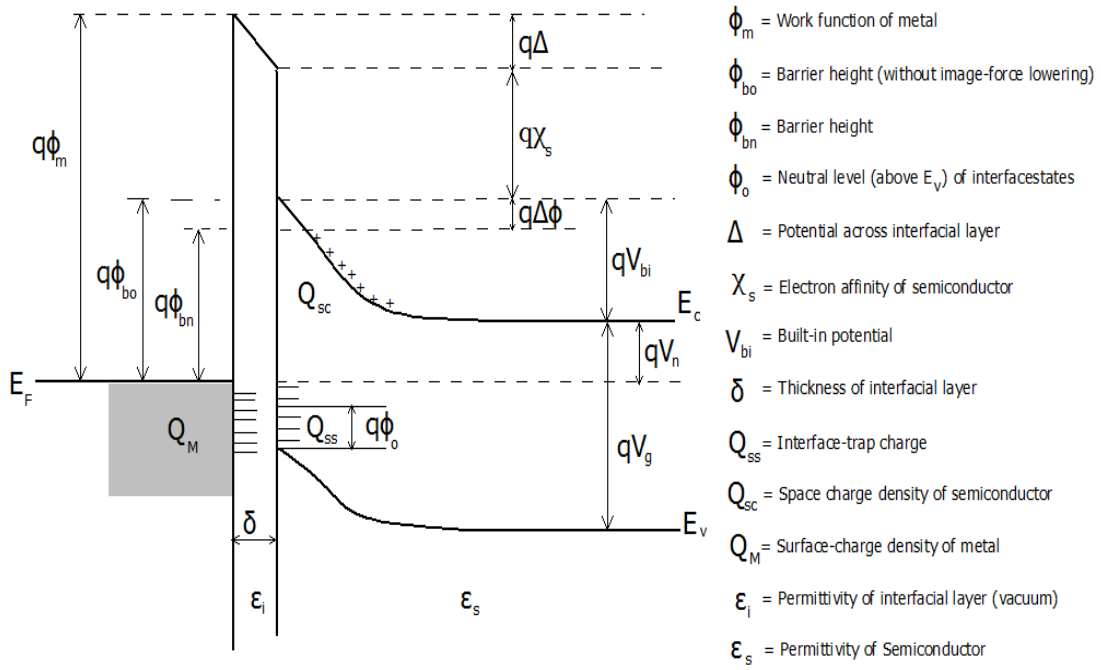

Fig. 3.1: Energy- band diagram of metal n-type semiconductor contact with an interfacial layer of the order of atomic distance.

3.1.2 Schottky Contacts

In metal-semiconductor contact, a Schottky contact is rectifying when conducting in the forward bias mode and allowing a negligible or no current in the reverse bias. Assume there are no surfaces and interface states present in the band edge and the Fermi energy of the metal as presented in Fig. 3.2.

The barrier height (ϕ_{bn}) of an ideal Schottky contact is simply the difference between the metal work function ϕ_m and the electron affinity (χ_s), given by for n-type semiconductor as in Fig. 3.1 [43].

$$\phi_{bn} = \phi_m - \chi_s \qquad (3.1)$$

and for a p-type semiconductor, the barrier height can also be written as,

$$\phi_{bp} = \phi_s - \phi_m \qquad (3.2)$$

where ϕ_s is the semiconductor work function. The barrier heights obtained from this method are said to be ideal, excluding real contacts, chemical reactions, interfacial layers and surface states affect the size of the barrier height. The latter mentioned effects alter the barrier height, making it difficult to obtain good rectifying metal semiconductor contacts on the ZnO [42].

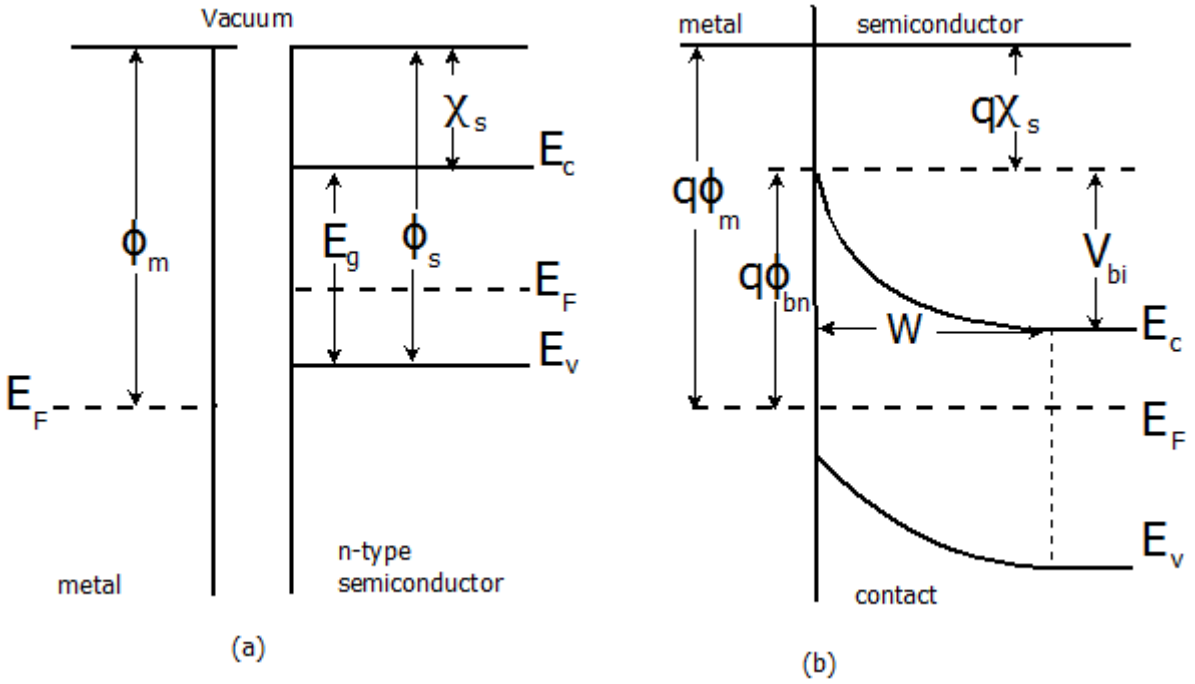

Fig. 3.2: Schematic diagrams of a Schottky contact to n-type semiconductor (a) before contact and (b) equilibrium band diagram for the contact.

3.1.3 Image-force lowering

The application of an electric field causes the image-force-induced lowering of the potential energy for charge carrier emission. Consider an electron, in vacuum, at a distance *x* from a metal surface. A positive charge will be induced on the metal at a distance -*x* from its surface and will give rise to an attractive force between the two, known as the image force. This force has associated with it an image potential energy which corresponds to the potential energy of an electron at a distance *x* from the metal. When an external field is applied, together these two energy components have the effect of lowering the Schottky barrier. Thus at high fields, the Schottky barrier is considerably lowered [44]. Fig. 3.3 shows the effects of the barrier lowering on the band diagram of metal-semiconductor contact.

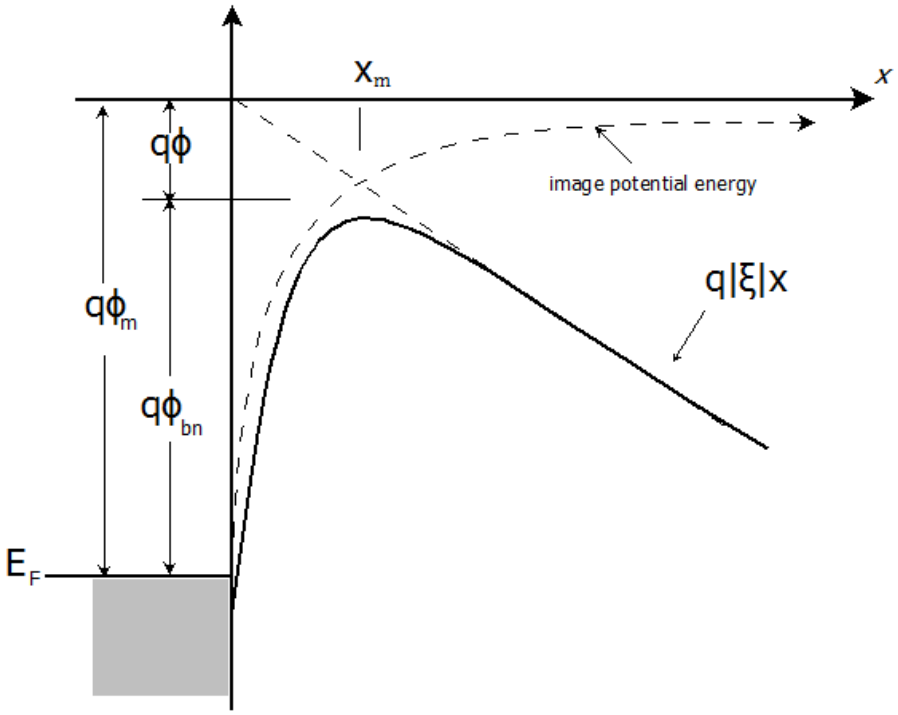

Fig. 3.3: Energy-band diagram between a metal surface and vacuum the effective barrier is lowered when an electric field is applied on the surface. The lowering is due to the combined effects of the field and the image force [42].

The work done on the electron when it is transferred from infinite to a point x is given by,

$$PE(x) = \int_{\infty}^{x} F dx = \frac{q^2}{16\pi\varepsilon_0 x} \tag{3.3}$$

Eq. 3.3 corresponds to the potential energy of an electron at distance x from the metal. The potential energy as a function of distance measured from the surface of the metal, under applied external electric field, given by,

$$PE(x) = \frac{q^2}{16\pi\varepsilon_0 x} + q|\xi|x \tag{3.4}$$

where ξ is the electric field strength. The image force lowering, and the location are obtained when $dPE(x)/dx = 0$ or

$$\Delta\phi = \sqrt{\frac{q}{4\pi\varepsilon_0}} = 2|\xi|x_m \tag{3.5}$$

and

$$x_m = \sqrt{\frac{q}{16\pi\varepsilon_0|\xi|}} \tag{3.6}$$

where the field due to the image force is equal and opposite to the field in the depletion region, the resultant electric field vanishes at the maximum potential energy at a position x_m. Assume that no interfacial layers are present between a metal and semiconductor, when applying the image-force lowering on metal-semiconductor contacts the image charge move to position x_m in the semiconductor. Substituting the permittivity of free space by the permittivity of the semiconductor, ε_s also the electric field by the maximum field at the interface, the Schottky effect is given by [40],

$$\Delta\phi = \sqrt{\frac{q\xi}{4\pi\varepsilon_s}} \tag{3.7}$$

where ε_s has a different value from the semiconductor static permittivity. The static permittivity value is determined by the emission process, the electron transit time from the metal-semiconductor interface to the barrier maximum, x_m is shorter than the dielectric relaxation time, the semiconductor medium rate of polarization determines the static value. Under different bias conditions on the metal-semiconductor contacts, the barrier lowering is influenced by the applied electric field, thus the different values of the barrier lowering.

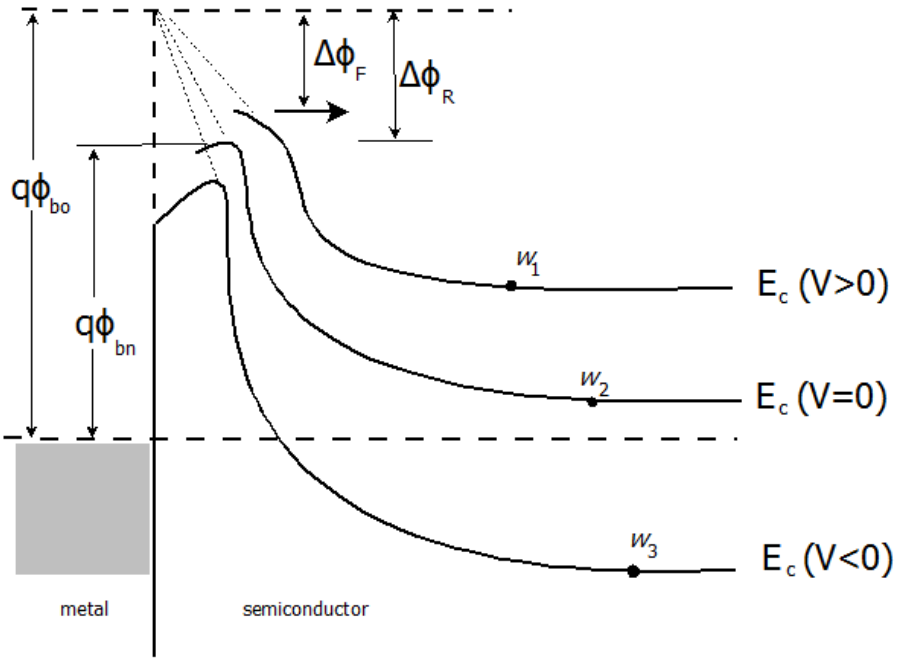

Fig. 3.4: Energy–band diagram incorporating the Schottky effect under different biasing conditions on a metal semiconductor contact. Where $q\phi_{bo}$ is the intrinsic barrier height, $q\phi_{bn}$ is the barrier height at thermal equilibrium, $\Delta\phi_F$ and $\Delta\phi_R$ the barrier lowering under forward and reverse bias, respectively [42].

Fig. 3.4 shows the energy diagram of a Schottky effect for a metal on n-type semiconductor under different biasing conditions. Note that for forward bias ($V > 0$), the image force and the field are smaller and the barrier height $q\phi_{bo} - q\Delta\phi_F$ is slightly larger than the barrier height at zero bias of

$$q\phi_{bn} = q\phi_{bo} - q\Delta\phi \tag{3.8}$$

For reverse bias ($V_r < 0$), the barrier height $q\phi_{bo} - q\Delta\phi_R$ is slightly smaller. In effect, the barrier height becomes bias dependent.

3.1.4 Ohmic contacts

In metal-semiconductor contact that has a negligible junction resistance relative to the total resistance of a semiconductor device is known as an ohmic contact. This contact should be such that no potential exist between the metal and semiconductor [45]. A good quality ohmic contact should not perturb the device performance and can supply the required current with a voltage drop that is sufficiently small compared with the drop across the active region of the device. An ideal metal semiconductor ohmic contact, occurs when there is unimpeded transfer of majority carriers from the semiconductor to the metal. The specific contact resistance, R_c is an important parameter in characterising the ohmic contact is given by [6]

$$R_c = \left(\frac{dJ}{dV}\right)^{-1}_{v=o} \tag{3.9}$$

Here R_c can be derived analytically by a computer numerical simulation to determine the dominant transport mechanism.

In Fig. 3.5 where the $\phi_s > \phi_m$ electrons move from the metal to the semiconductor thereby aligning the Fermi levels to reach equilibrium. This lowers the potential barrier, so the electrons in the semiconductor have higher energy to surmount the barrier by a small voltage. In addition, electronegativity of the metal and the surface roughness of the semiconductor affect the ohmic contact quality. The dependence of the contact on electronegativity have been studied on metal-ZnO contacts by Reddy *et al* [16]. Since aluminium has a low electronegativity, it acts as a source of electrons and it has a tendency of releasing them because of weak bonds that exist among them. This causes the current flowing through the junction to follow thermionic emission (TE) mechanism model [45].

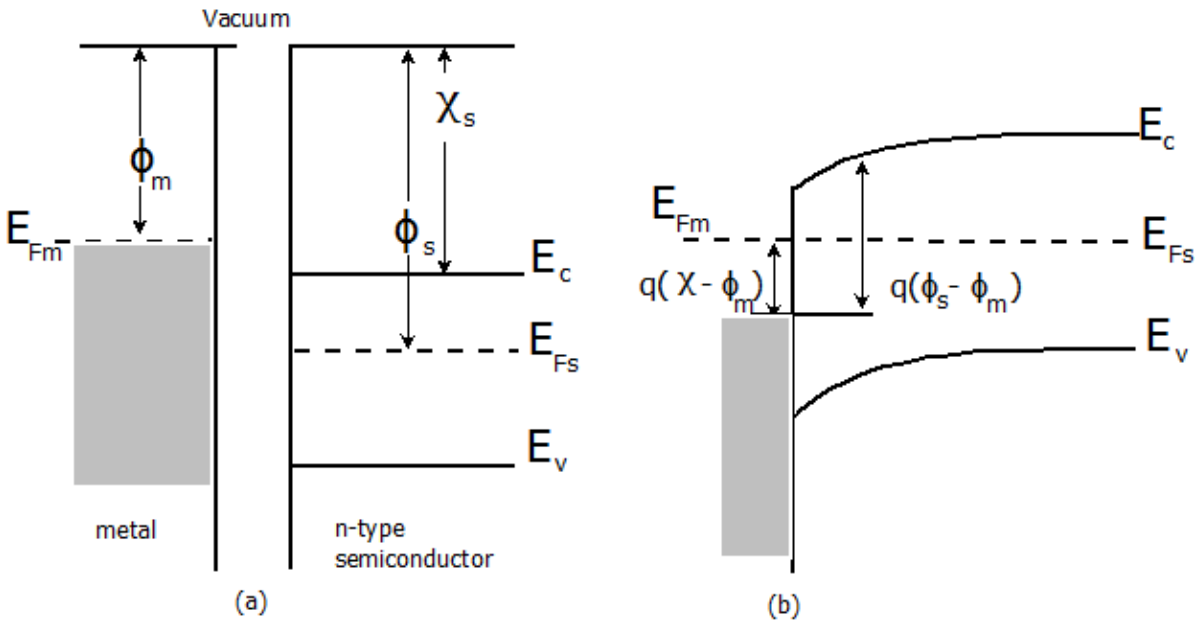

Fig. 3.5: Schematic diagrams of an ohmic contact to n-type semiconductor (a) before contact $\phi_s > \phi_m$ and (b) equilibrium band diagram for the contact.

3.2 Current transport mechanisms

3.2.1 Thermionic emission

Current flow from metal into a semiconductor in the thermionic emission model is solely dependent on the barrier height. Electrons need sufficient energy to surmount the barrier from the semiconductor to the metal and the current density J_{sm} traversing in the *x*-direction [42]

$$J_{sm} = \int_{E_{Fn}+\phi_{bn}}^{\infty} q v_x dn \qquad (3.10)$$

where $E_{Fn} + \phi_{bn}$ is the minimum energy required for electrons to surmount the barrier height and v_x is the carrier velocity in the direction of transport. The electron density in an incremental energy range is given by [42, 44]

$$dn = N(E)F(E)dE$$

$$\approx \frac{4\pi(2m^*)^{3/2}}{h^3}\sqrt{E - E_c}\, exp(-\frac{E-E_c+q\phi_n}{kT})\, dE \qquad (3.11)$$

where *N(E)* is the density of states, *F(E)* is the distribution function and *m** is the effective mass of electrons. If we postulate that all the energy of the electrons in the conduction band is kinetic energy, then

$$E - E_c = \frac{1}{2}m^* v^2$$

$$dE = m^* v dv$$

$$\sqrt{E - E_c} = v\sqrt{m^*/2} \tag{3.12}$$

Substituting Eq. 3.11 into Eq. 3.10 gives

$$dn \approx 2\left(\frac{m^*}{h}\right)^3 exp\left(\frac{q\phi_n}{kT}\right) exp\left(-\frac{m^*v^2}{2kT}\right)(4\pi v^2 dv) \tag{3.13}$$

using Eq. 3.13 to determine the number of electrons per unit volume that have velocities between v and $v+dv$, distributed over all directions. If the velocity is resolved into its components along the axes with the x-axis parallel to the transport direction, then

$$v^2 = v_x^2 + v_y^2 + v_z^2 \tag{3.14}$$

with the transformation $4\pi v^2 dv = dv_x dv_y dv_z$, we get from Eq. 3.10, 3.13 and 3.14

$$J_{sm} = \left(\frac{4\pi q m^* k^2}{h^3}\right) T^2 exp\left(-\frac{q\phi_n}{kT}\right) exp\left(-\frac{m^* v_{ox}^2}{2kT}\right) \tag{3.15}$$

where v_{ox} is the minimum velocity required surmount the barrier height in the x-direction and is given by

$$\frac{1}{2} m^* v_{ox}^2 = q(V_{bi} - V) \tag{3.16}$$

Substituting Eq. 3.16 into 3.15 gives

$$\begin{aligned} J_{sm} &= \left(\frac{4\pi q m^* k^2}{h^3}\right) T^2 exp\left(-\frac{q(\phi_n - V_{bi})}{kT}\right) exp\left(\frac{qV}{kT}\right) \\ &= A^* T^2 exp\left(-\frac{q\phi_b}{kT}\right) exp\left(\frac{qV}{kT}\right) \end{aligned} \tag{3.17}$$

Here A^* is the effective Richardson constant for thermionic emission and ϕ_b is the barrier height.

As the barrier height for electrons moving from the metal into the semiconductor remains the same under bias, the current flowing into the semiconductor is thus unaffected by the applied voltage. At thermal equilibrium, the current flowing from the metal to the semiconductor should be the same as the current flowing from semiconductor to the metal, if and only if $V = 0$. The corresponding current density obtained from Eq. 3.17 is given by, when $V = 0$

$$J_{ms} = -A^* T^2 exp\left(-\frac{q\phi_b}{kT}\right) \tag{3.18}$$

The negative sign implies that the current is flowing from the metal to the semiconductor. The total current density flowing over the barrier is given by the sum of the current flow from semiconductor into metal or metal into semiconductor:

$$J_{total} = J_{ms} + J_{sm}$$
$$= \left\{A^* T^2 exp\left(-\frac{q\phi_b}{kT}\right)\right\}\left\{exp\left(\frac{qV}{kT}\right) - 1\right\}$$
$$= J_s\left\{exp\left(\frac{qV}{kT}\right) - 1\right\} \quad (3.19)$$

where J_s the saturation current given by:

$$J_s = \left\{A^* T^2 exp\left(-\frac{q\phi_b}{kT}\right)\right\} \quad (3.20)$$

The total current in Eq. 3.19 is also known as the Schottky diode equation, which predicts an exponential dependence of the current density on both applied forward bias and temperature. Since J_s depends exponentially on the barrier height, a large barrier height is required to reduce the value of J_s in a Schottky diode.

3.2.2 Quantum mechanical tunneling

Basically, in heavily doped semiconductors and low temperature operation, tunneling current is usually the dominant transport mechanism [21]. At low temperatures, the Fermi level of the semiconductor moves up thereby reducing the barrier height. Considering the wave nature of electrons, the barrier becomes very thin and compatible with the wavelength of these electrons, i.e. their energies will be large enough to allow tunneling from the semiconductor to the metal as their energies will be too low for them to cross over the barrier. Tunneling is also promoted by the existence of the interface states on the metal/semiconductor contacts. These interface states lead to the existence of a Gaussian distribution of the barrier heights, i.e. low and high barriers embedded on a uniform barrier [42]. As the current flows through such a contact, charge carriers will follow a path which is easier for them to cross the barrier, as a result, they will tunnel through the low barrier area resulting in tunneling current.

According to Rhoderick [43], tunneling of carriers in heavily doped semiconductors at low temperatures modifies the usual TE process into field and thermionic field emission. While field emission (FE) is a pure tunneling process, thermionic field emission (TFE) is tunneling of thermal excited carriers which sees a thinner barrier than FE [42]. Considering high doping densities of a semiconductor, the barrier is sufficiently narrow at or near the bottom of the conduction band for electrons to tunnel directly. Raising the temperature, but not high enough to give the electrons enough energy to go over the barrier, excites carriers to high energies, increasing the tunneling probability very rapidly and charge carriers will ‘see’ a thinner and sufficiently narrow reduced barrier to easier tunneling [43]. However, the number of excited

electrons decrease rapidly with increasing energy and the contribution to the current by carrier with energies above the bottom of the conduction band becomes maximum. This mechanism is referred to as thermionic field emission (TFE) as shown in Fig. 3.6. In the case where tunneling current dominants the current flow, the transmission coefficient is given by [42]

$$T(\eta) \backsim exp\left(\frac{q\phi_{bn}}{E_{00}}\right) \tag{3.21}$$

where E_{00} is the characteristic energy level given by

$$E_{00} = \frac{q\hbar}{2}\sqrt{\frac{N_D}{\varepsilon_s m^*}} \tag{3.22}$$

The tunneling current density is given by

$$J_t = exp\left(-\frac{q\phi_{bn}}{E_{00}}\right) \tag{3.23}$$

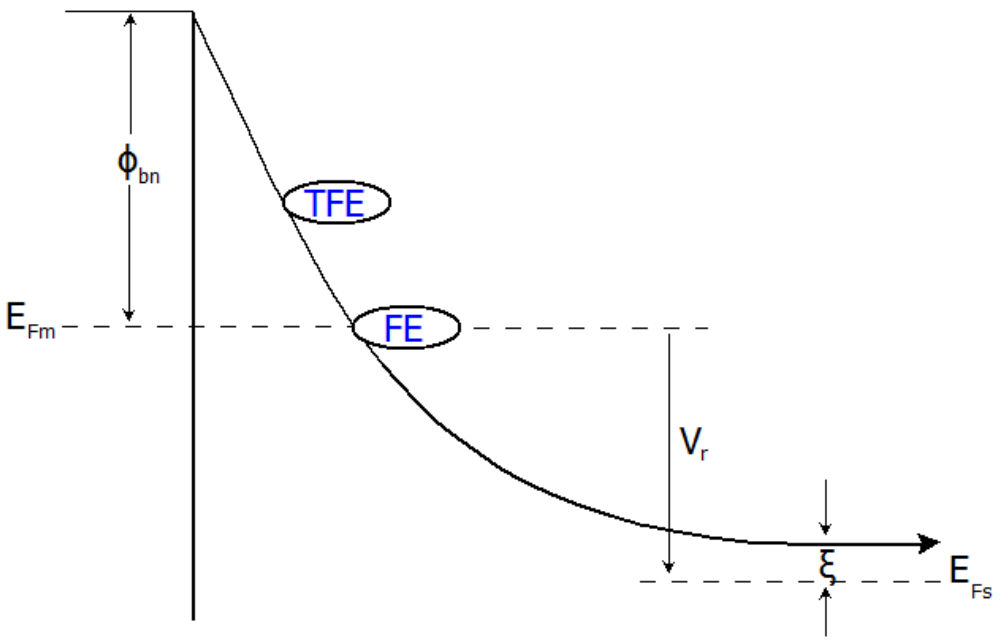

Fig. 3.6: Schematic band diagram under forward bias featuring thermionic field emission (TFE) and field emission (FE) transport mechanisms.

3.2.3 Generation-recombination

Generation-recombination processes in a semiconductor occurs when electrons and holes can either be generated or recombined within a given volume, thereby changing the local carrier concentration. These events change the local carrier concentration, the entire semiconductor must always remain in the space charge neutral. Therefore, the requirement leads to the injection and extraction of charge at the contacts. The process takes place in one of the two ways explained below. In the case where transition happens from band to band, an electron from the conduction band recombines with a hole in the valence band [43]. The other case can be describe by the localised states, which exist in the forbidden gap within the space charge region, that can either catch or emit electrons or holes. Under reverse bias conditions, the dominant generation-recombination process is the formation of an electron hole pair as shown in Fig. 3.7.

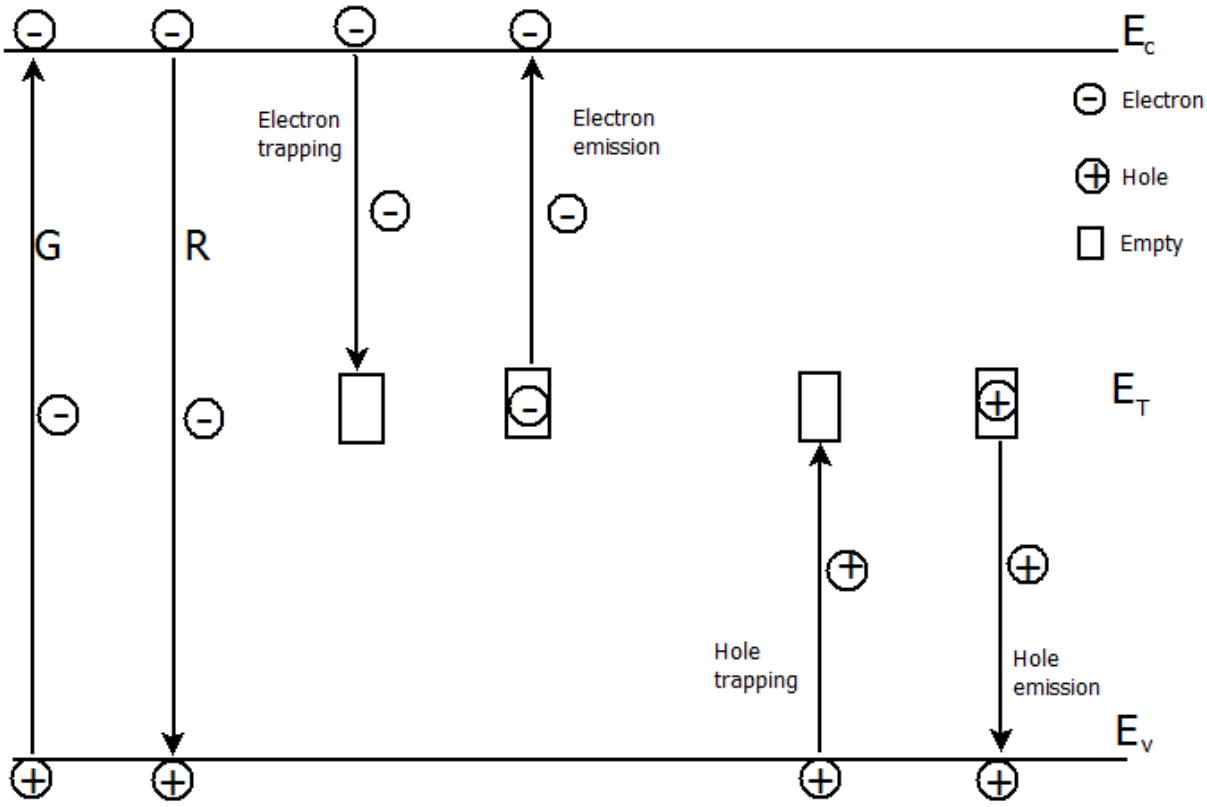

Fig. 3.7: Schematic diagram of generation-recombination(R-G) transport mechanism in a semiconductor [43].

Under forward bias characteristics, the dominant process is the destruction of an electron-hole pair. This occurs when an electron in the conduction band loses energy and falls into the recombination centre and then into the valence band. The most effective localization trap centres are those with high energies lying near the centre of the forbidden gap. The theory of

current due to such recombination centre is similar to that for p-n junctions and was predicated by the Shockley, Hall and Read (S-H-R) model where the current density at low forward bias is given by [43].

$$J_r = J_{r0}\, exp\left(\frac{qV}{kT}\right)\left\{exp\left(\frac{qV}{kT}\right) - 1\right\} \qquad (3.24)$$

where $J_{r0} = qn_i w/2\tau_r$, n_i is the intrinsic electron concentration, proportional to $\exp(qE_g/2kT)$, w is the depletion width and τ_r is the life time within the depletion width. The rate G describes the number of generated electron-hole pairs per unit time and volume. As generation processes play an important role in advanced electronic devices (laser, light emitting diodes (LED)), the opposite process to generation, called recombination appears in all semiconductor-based devices more or less [46].

3.4 Effects of surface states

According to Schottky-Mott theory, the barrier height is dependent of the metal work function ϕ_m. Although, experimentally the barrier height is less affected by the metal work function and further suggesting that under certain conditions the barrier height may be independent to the metal chosen. The discrepancy was explained by Bardeen to be associated with surface state [47]. Surface states are electronic states often found on the surface of a semiconductor formed due to a sharp termination of solid material that ends with a surface. This results in the formation of incomplete covalent bonds at the surface leading to a change of the electronic band structure from the bulk material to vacuum. In the semiconductor band gap electron energy levels are now created which can be either donor states or acceptor states based on whether or not they are neutral or charged when occupied. The surface of the semiconductor has incomplete covalent bonds, which are completed during deposition of metals. Therefore, some electrons from the valence band will fill the vacant states in the semiconductor atoms and maintain charge neutrality at the semiconductor surface, while trying to establish equilibrium. This process will lead to pinning of the Fermi levels. The surface state charge density Q_{ss}, given by [42],

$$Q_{ss} = -qD_s E_g - q\Phi_0 - q\Phi_{Bn} - q\Delta\Phi \qquad (3.25)$$

Here D_s is the density of surface states, E_g is the energy band gap and Φ_0 is the neutral level at the interface states as shown in Fig. 3.1.

3.5 Fermi level pinning

Fermi level pinning in a semiconductor contacting a metal is essentially independent of the metal even for large variation in the work function of the metal during band bending. In the existence of surface states, the electrons from the valance band of the semiconductor will be trapped by these vacant states until the Fermi level coincides with the level to which the surface states are filled. A natural surface depletion of the semiconductor occurs and at the same time, a potential across the semiconductor is establish resulting in a barrier height independent of the metal work function. From the Bardeen theory, the resulting barrier height and the built-in potential are given by [21]

$$\Phi_B = \Phi_m - \Phi_{so} + qV_i \tag{3.26}$$

$$V_{bi} = \frac{\Phi_m + \chi_s}{q} + V_i \tag{3.27}$$

where χ_s is the electron affinity of semiconductor, V_i is the voltage drop due to the surface states and Φ_{so} is the work function of semiconductor.

Chapter 4

Electrical characterization techniques

4.1 Introduction

Zinc Oxide (ZnO) has gained a lot of global interest in the research community because of its direct and wide band gap of 3.37 eV. It has a larger exciton binding energy of 60 meV and hence a high efficiency in excitonic emission [48, 49]. It also has superior electronic properties such as high breakdown voltage, high electron saturation velocity, high thermal conductivity and is very resistant to high-energy radiation, making it a very suitable candidate for space or around nuclear reactors applications [5]. ZnO has found applications in a number of semiconductor electronic devices such as in the ultraviolet, blue-range optoelectronics, lasers, photovoltaics, field effect transistors, microwave diodes and gas sensors [50]. Hence, different techniques have been used to electrically characterize ZnO. In this section a detailed outline of current-voltage (*IV*) and capacitance-voltage (*CV*) measurements, which were used to characterize parameters such as electron mobility, Schottky barrier height, Schottky contact quality, series resistance, reverse leakage and forward current is presented. Also, deep level transient spectroscopy (DLTS) is a high frequency transient capacitance technique, which has proven to be a very useful tool to probe the defect located far from the surface of the semiconductor since it was discovered by Lang [13] is discussed. Lastly, the recently developed high-resolution Laplace DLTS (L-DLTS), which greatly enhances the resolution and spectroscopic nature of the capacitance based defect characterization tools is presented [21].

4.2 Current-voltage and Capacitance-voltage Measurements

4.2.1 Current-voltage measurements

Consider Fig. 3.1 showing an energy-band diagram of a metal and n-type semiconductor contact. The motion of the electrons over the barrier into the metal is governed by the usual mechanisms of drift and diffusion. The electron concentration on the semiconductor side of the boundary is given by [42]:

$$n = N_c \, exp\{-q\,(\phi_b - V)/kT\} \qquad (4.1)$$

where N_c is the density of states.

The current density due to motion of the electrons from the semiconductor into the metal is

$$J_{sm} = \frac{pqN_c v}{4} exp\{-q(\phi_b - V)/kT\} \quad (4.2)$$

where v is the average thermal velocity of the electrons and p is the probability of electrons tunneling through the insulating layer. In addition, there is a flow of electrons from the metal to the semiconductor and since the barrier is seen unchanged from the metal with applied bias, it follows that

$$J_{ms} = \frac{pqN_c v}{4} exp(-q\phi_b/kT) \quad (4.3)$$

The total current flowing is given by,

$$J = J_{sm} - J_{ms}$$

$$= \frac{pqN_c v}{4} exp\left(\frac{-q\phi_b}{kT}\right)\left\{exp\left(\frac{qV}{kT}\right) - 1\right\} \quad (4.4)$$

Consider that p approaches unity as the insulating layer becomes thinner and substituting

$$N_c = 2(2\pi m^* kT/h^2)^{3/2} \quad (4.5)$$

Eq. 4.4 becomes

$$J = A^* T^2 exp\left(\frac{-q\phi_b}{kT}\right)\left\{exp\left(\frac{qV}{kT}\right) - 1\right\} \quad (4.6)$$

Assume that in Eq. 4.6, the barrier height is independent of bias. However, there are several reasons why the barrier height may depend on the electrical field in the depletion region and hence on the applied bias. Even for ideal Schottky contact, the barrier height is reduced by an amount of $\Delta\phi_{bi}$ because of image force. Hence, the effective barrier of electrons must surmount $\phi_e = \phi_b - \Delta\phi_{bi}$. In the case where the interfacial layer is present, ϕ_b also depends on the bias and therefore the effective barrier height is

$$\phi_e = \phi_{bo} - (\Delta\phi_{bi})_o + \beta V \quad (4.7)$$

where β is a constant, then Eq. 4.6 can be written as

$$J = J_s exp\left(\frac{qV}{nkT}\right)\left\{exp\left(\frac{qV}{kT}\right) - 1\right\} \quad (4.8)$$

where J_s is the saturation current density of thermionic emission given by,

$$J_s = A^* T^2 exp\left(\frac{-q\phi_b}{kT}\right) \quad (4.9)$$

Eq. 4.8 gives the current density of an ideal diode. For a non-ideal diode, the series resistance, R_s and the ideality factor, n need to be factored into Eq. 4.8, then

$$J = J_s \, exp\left[\frac{qV - IR_s}{nkT}\right]\left\{1 - exp\left[-\frac{qV - IR_s}{kT}\right]\right\} \qquad (4.10)$$

The ideality factor is calculated as the gradient of the slope of linear region of the semi-logarithmic *IV* plot and is given by

$$n = \frac{q}{kT}\left(\frac{dV}{d\ ln\ I}\right) \qquad (4.11)$$

and R_s is obtained from the deviation of the semi logarithmic *IV* plot linearity at high currents as

$$R_s = \frac{\Delta V}{\Delta I} \qquad (4.12)$$

4.2.2 Barrier Height Inhomogeneities

Barrier height inhomogeneity is the modification of the barrier height in metal-semiconductor contact. Several researchers [51, 52] referred to the situation in which the contact consists of low and high barrier areas at the interface mainly due to the formation of different insulative, oxide layer thickness between the metal and the semiconductor.

In addressing the observed inhomogeneities in the Schottky barrier diodes, which deviates from classical TE theory, some researchers have considered a system of discrete regions of low barrier areas imbedded in a high background uniform barrier [52-54]. Werner and Guttler [51] developed an analytical model, to explained the fluctuations by assuming the Gaussian distribution of the barrier heights with a mean value $\overline{\Phi}_b$ and standard deviation σ_s, which can be given by

$$P(\emptyset_b) = \frac{1}{\sigma_s\sqrt{2\pi}} exp\left[-\frac{(\Phi_b) - \overline{\Phi}_b}{2\sigma_s^2}\right] \qquad (4.13)$$

where $1/\sigma_s\sqrt{2\pi}$ is the normalization constant of the Gaussian barrier height distribution. The total *I(V)* across a Schottky diode containing a barrier inhomogeneities can be expressed as [53]:

$$I(V) = \int_{-\infty}^{+\infty} I(\Phi_b, V) P(\Phi_b) d\phi_b \qquad (4.14)$$

where $I(\Phi_b, V)$ is the current at a bias *V* for a barrier height based on the ideal thermionic emission-diffusion (TED) theory and $P(\Phi_b)$ is the normalization distribution function giving the probability of accuracy for the barrier height. Substituting $Eq.$ (4.4) for $I(\Phi_b, V)$ and Eq. (4.13) for $P(\Phi_b)$ in Eq. (4.14), we obtain the current *I(V)* through the Schottky barrier at a forward bias V but with a modified barrier as [53]:

$$J(V) = J_s \, exp\left(\frac{qV}{n_{ap}kT}\right) x \left[1 - exp\left(-\frac{qv}{kT}\right)\right] \quad (4.15)$$

with

$$J_s = AA^{**}T^2 exp\left(-\frac{q\Phi_{ap}}{kT}\right) \quad (4.16)$$

where A^{**} is the modified Richardson constant, n_{ap} and Φ_{ap} are the apparent ideality factor and apparent barrier height at zero bias, respectively, given by [55]

$$\Phi_{ap} = \bar{\Phi}_{b\,(T=0)} - \frac{q\sigma_{so}^2}{2kT} \quad (4.17)$$

and

$$\left(\frac{1}{n_{ap}} - 1\right) = \rho_2 - \frac{q\rho_3}{2kT} \quad (4.18)$$

It is assumed that the mean Schottky barrier height, $\bar{\Phi}_b$ and the standard deviation, σ_s are linearly bias-dependent on Gaussian parameters, such that $\bar{\Phi}_b = \bar{\Phi}_{bo} + \rho_2 V$ and a standard deviation $\sigma_s = \sigma_{so} + \rho_3 V$, where $\bar{\Phi}_{bo}$ is the mean barrier height at temperature T = 0 K, ρ_2 and ρ_3 are voltage coefficients which may depend on temperature, quantifying the voltage deformation of the barrier height distribution [56]. The temperature dependence of σ_s is small and therefore can be neglected. The decrease of zero-bias barrier height is caused by the existence of Gaussian distribution and the extent of influence is determined by the standard deviation itself [53, 56].

The current transport of electrons across Schottky barrier is affected by the presence of barrier inhomogeneities. At low temperatures, charge carriers do not have enough energy to surmount the energy barriers; the dominant transport mechanism of electrons is tunneling. The tunneling of the electrons through low barrier areas will cause a deviation of the barrier height from the actual value obtained for a homogeneous barrier at the MS interface [57]. A linear fit for the apparent ideality factor, should be observed if Eq. 4.11 is obeyed. In the low temperature region, the decrease in Φ_{bo} is caused by the existence of the Gaussian distribution and the extent of influence is determined by the standard deviation itself. In addition, the effect is particularly significant at low temperatures [56]. The fitting of the experimental data using Eq. 4.17 and 4.18 gives Φ_{ap} and n_{ap} at zero bias, respectively. Thus, fit of Φ_{ap} versus $q/2kT$ is linear, where Φ_{bo} and σ_{so} are obtained from the intercepts and the slope, respectively. The smaller the value of the standard deviation σ_{so}, the more homogeneous the barrier height is and the better the diode rectifying performance [56].

4.2.3 The modified Richardson constant

To address these observed irregularities, one can correct for the barrier height inhomogeneities according to the Gaussian distribution of the barrier height, can therefore modify Eq. 4.16 to give [51]:

$$J_s = AA^{**}T^2\, exp\left[-\frac{q\Phi_{ap}}{kT} + \frac{q^2\sigma_{so}^2}{2k^2T^2}\right] \qquad (4.19)$$

and

$$ln\left(\frac{J_s}{T^2}\right) - \left(\frac{q^2\sigma_{so}^2}{2k^2T^2}\right) = ln(AA^{**}) - \frac{q\Phi_{ap}}{kT} \qquad (4.20)$$

A plot of the modified $ln\ (J_s/T^2) - (q^2\sigma_{so}^2/2k^2T^2)$ versus $1000/T$ plot according to Eq. 4.20 should give a straight line with a slope directly yielding the mean barrier height and the intercept ln (AA^{**}) relating to the modified Richardson constant A^{**} for a given diode area A.

4.3 Capacitance-voltage measurements

Considering the Schottky-Mott model on an n-type semiconductor with Schottky contact and, where the metal work function Φ_m is greater than the electron affinity χ of the semiconductor. As seen in Fig. 3.2.a before the metal and semiconductor are in contact. Where q is the elementary charge, E_F is the Fermi level, E_c is the conduction band and E_v is the valence band minimum. If an n-type semiconductor with a density of donors N_D is used, a similar model can be used in p-type materials. When the metal and semiconductor are brought into contact, electrons in the semiconductor side will occupy the energetically more favourable states in the metal. As a result, the donor states the electrons formally occupied on the semiconductors side are empty and with a positive charge. In the semiconductor domain of the contact a space charge region is formed and a potential barrier is formed at the contact. At equilibrium, the net flow of the electrons from the semiconductor to the metal is zero. This happens, when the barrier hindering electron flow from the metal to the semiconductor is equal to that for electron flow from the semiconductor to the metal. This barrier is given by $\phi_B = \phi_m - \chi_s$. The charge density $\rho(x)$ in the depletion region where there are no electrons in the conduction band given by qN_D. If the depletion width is w, the charge density in the semiconductor is given by

$$\rho(x) = \begin{cases} qN_D if x \le w \\ 0 \quad if x > w \end{cases}$$

and the potential distribution within the semiconductor depletion region is [42]

$$\phi(x) = \frac{qN_D}{\epsilon_0\epsilon_s}\left(wx - \frac{x^2}{2}\right) - \frac{\phi_B}{q} \quad (4.21)$$

with the depletion width *w* given by:

$$w = \sqrt{\frac{2\epsilon_0\epsilon_s}{qN_D}(V_{bi} - V - kT/q)} \quad (4.22)$$

The *kT/q* arises from the contribution the majority carrier distribution function. The space charge per unit area Q_s of the semiconductor is

$$Q_s = qN_D w = \sqrt{2\epsilon_0\epsilon_s qN_D(V_{bi} - V - kT/q)} \quad (4.23)$$

From which the depletion layer capacitance per unit area *C* is obtained:

$$C \equiv \frac{dQ_s}{dV} = \sqrt{\frac{\epsilon_0\epsilon_s qN_D}{2(V_{bi} - V - kT/q)}} = \frac{\epsilon_0\epsilon_s}{w} \quad (4.24)$$

The capacitance of a Schottky diode is measured by applying an alternating test voltage of frequency (f) to the Schottky diode. This causes a periodic charge and discharge of donors at the end of the depletion region and with that a flow of charges. The charging and discharge regions depend on the amplitude of the alternating test voltage. Additional to the alternating test voltage DC bias can be applied to the diode shifting the region of charging and discharging. The *CV* measurements determine the capacitance of and the doping density for different regions under the semiconductor surface. The net doping density profile is determined by [47],

$$N_D(w) = -\frac{2}{q\epsilon_0\epsilon_s}\left(\frac{dC^{-2}}{dV}\right)^{-1} \quad (4.25)$$

and

$$w = \frac{\epsilon_0\epsilon_s}{C} \quad (4.26)$$

The slope (dC^{-2}/dV) has different signs for p-type and n-type semiconductors, respectively. Further, from the *CV* measurements the barrier height can be deduced from the intersection of the extrapolated C^2 versus *V* plot with the voltage axis the built-in potential V_{bi} is determined. The barrier height calculated from the *CV* measurement is given by

$$\phi_{b,CV} = qV_{bi} + \frac{kT}{q} ln\left(\frac{N_c}{N_D}\right) + \frac{kT}{q} - \phi_i \quad (4.27)$$

where ϕ_i is the lowering of the barrier due to image force lowering, which was neglected so far. ϕ_i is given by

$$\phi_i = \sqrt{\frac{q\varepsilon_{max}}{4\pi\epsilon_0\epsilon_s}} \tag{4.28}$$

where ε_{max} is the maximum electric field for given bias.

4.4 Deep level transient spectroscopy (DLTS)

The conventional DLTS is a powerful high frequency capacitance transient thermal scanning technique used for observing a wide variety of traps in semiconductors [13]. The technique can be used to investigate the depletion region of an ordinary p-n junction, Schottky diode, or MOS devices structure. The measurement process uses the change in the capacitance transient associated with the thermal emission of charge carriers from trap level to the thermal equilibrium after initial non-equilibrium condition in the space charge region. DLTS has a high sensitivity, good resolution, easy analysis of spectra, rapid scanning and capable of measuring over a wide range of depths in the forbidden gap and detect at shallow levels from below the conduction band [33].

From the scan of DLTS, the nature of each trap is outlined with either a positive peak or negative peak on a flat base line plotted as a function of temperature. The sign of each peak indicate whether it is due to a majority (e^-) or minority (h^+) trap and position of the peaks are determined by the instrument rate window and the thermal properties of the respective traps. From the DLTS measurements, there is a possibility to extract the thermal emission rate, activation energy, concentration profile and the capture cross section of each trap. In addition, the technique has the ability to identify the concentration profiles of the deep levels. In this section, the discussion is based on how the technique is used in the depletion region formed between the Schottky diode and semiconductor [10].

The width in the depletion region of the metal semiconductor contact, given by,

$$w = \sqrt{\frac{2\varepsilon_s}{qN_D}(V_{bi} - V_a)} \tag{4.29}$$

where ε_s is the semiconductor permittivity, V_{bi} is the built in potential of the junction, V_a is the externally applied voltage, q is the electronic charge and N_D is the density of the ionized impurities due to dopants and other defects with the levels in the bandgap. The corresponding junction capacitance is now given by [42],

$$C = \frac{A\varepsilon_s}{w} = A\sqrt{\frac{q\varepsilon_s N_D}{2(V_{bi}-V_a)}} \tag{4.30}$$

Here A is the cross-sectional area of the junction. The capacitance of the depletion region depends on the applied bias voltage and the dopant concentration as shown in Eq. 4.29 and 4.30. It is the sensitivity of the capacitance to change the charges in the depletion region that is exploited and forms the basis of DLTS [58].

In a case of the formation of a metal-semiconductor contact, a region depleted of charge carriers is formed. Assuming that the region is formed within the semiconductor band gap, using the depletion width approximation, the semiconductor is now divided into two distinct regions, i.e. the bulk region, which is electrical neutral and the space charge region, which is depleted of charge carriers. From Fig. 4.1 depicting a real junction, where a region λ lies between the truly depleted region and the bulk region. This region λ is defined as the distance between the depletion region edge and the point where the deep levels E_T crosses the Fermi level E_F.

Since the defect level typically lies much deeper in the band than the dopant level, the defect level intersects the Fermi level a distance λ shallower than the depletion region edge, as shown in Fig. 4.1. The result is that the DLTS measurement does not probe the region at the depletion region edge, but a region a distance λ shallower than the depletion region. This effect has to be taken into account when the DLTS technique is used to determine the depth profile of defects or the electric field experienced by the defects is calculated. Furthermore, during the transient, charges are removed a distance λ from the depletion region edge.

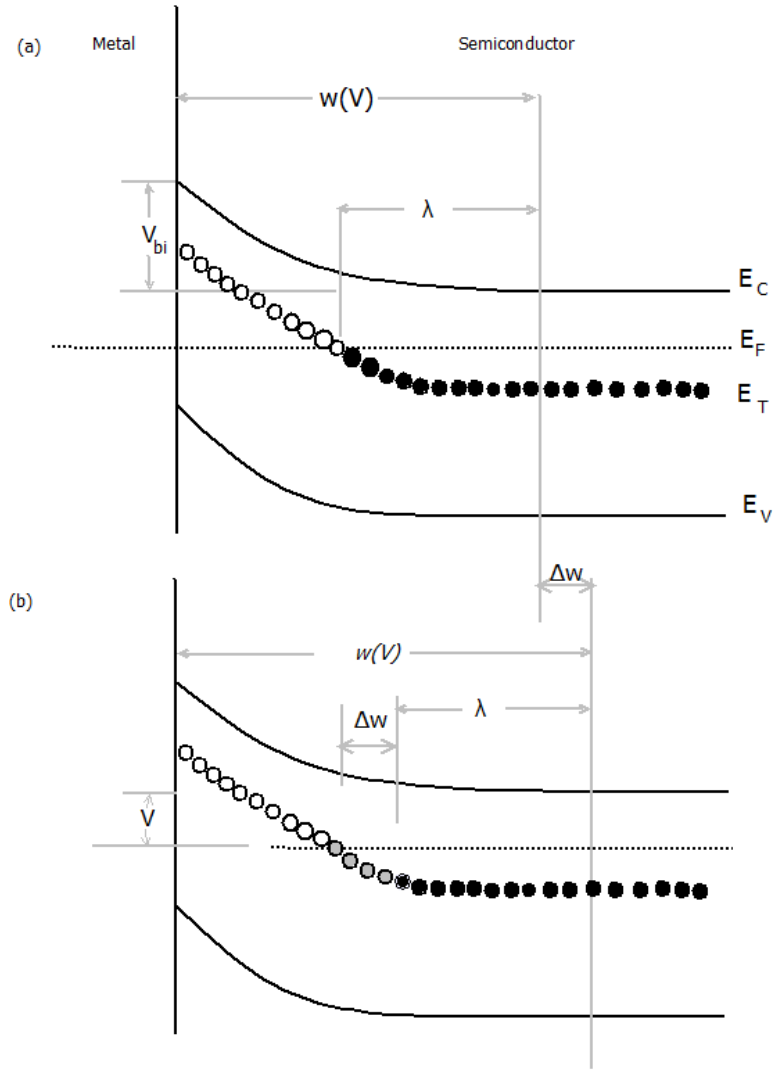

Fig.4.1: Filling (a) and subsequent emission (b) of electron from a deep level in the depletion region, assuming a constant Fermi level. In (a) the filling of the defect during the filling pulse is shown. Note that due to band bending and the depth of the defect level, the defect level is filled to a depth λ shallower than the depletion region edge. After the filling pulse, the width of the depletion region increase by an amount Δw. Carriers are now emitted from the band of defects with a width Δw a distance λ shallower than the depletion region edge.

Consider a Schottky barrier fabricated on n-type semiconductor. A similar results is expected for a p^+ -n junction as those presented below. Consider also an electron trap with density N_T, capture cross-section σ_n and the position $E_c - E_T$ below the conduction band edge. The thermal emission rate e_n of electrons from such a trap is given b,

$$e_n = \sigma_n \langle v_n \rangle N_c \, exp[-(E_c - E_T)/kT] \qquad (4.31)$$

where N_c is the density of states in the conduction band given by,

$$N_c = 2M_c[2\pi m_n^* kT/h^2]^{3/2} \qquad (4.32)$$

M_c is the number of equivalent conduction band minima, m_n^* is the electron effective mass and $\langle v_n \rangle$ is the thermal velocity for electrons, given by,

$$\langle v_n \rangle = (3kT/m_n^*)^{1/2} \qquad (4.33)$$

Fig. 4.2 illustrate energy band diagram and capacitance transient resulting from a majority carrier pulse. Under a reverse bias and steady state, (a), the deep levels under the Fermi level are assumed filled and those above are empty as governed by the Fermi distribution function. The empty deep levels in the band gap are indicated by empty squares. Assume the reduction of the applied voltage, by applying a positive going pulse (b), the depletion region width will decrease in magnitude and majority carriers will be captured by the traps at a rate given by,

$$C_n = \sigma_n \langle v_n \rangle n \qquad (4.34)$$

where n is the majority carrier density of the semiconductor. Consider a filling pulse, which is long enough to allow all the empty levels to be completely filled up. This leads to the increment of the capacitance due to the reduction of the depletion region. After removing the pulse (c), the filled states within the depletion region, above the Fermi level start emitting carriers with a characteristic rate into the conduction band where they are instantaneously swept away by the junction electric field (d). This thermal emission of the trap electrons where the junction sweeps them instantaneously into the conduction band is taken to be the majority carrier capacitance transient [6].

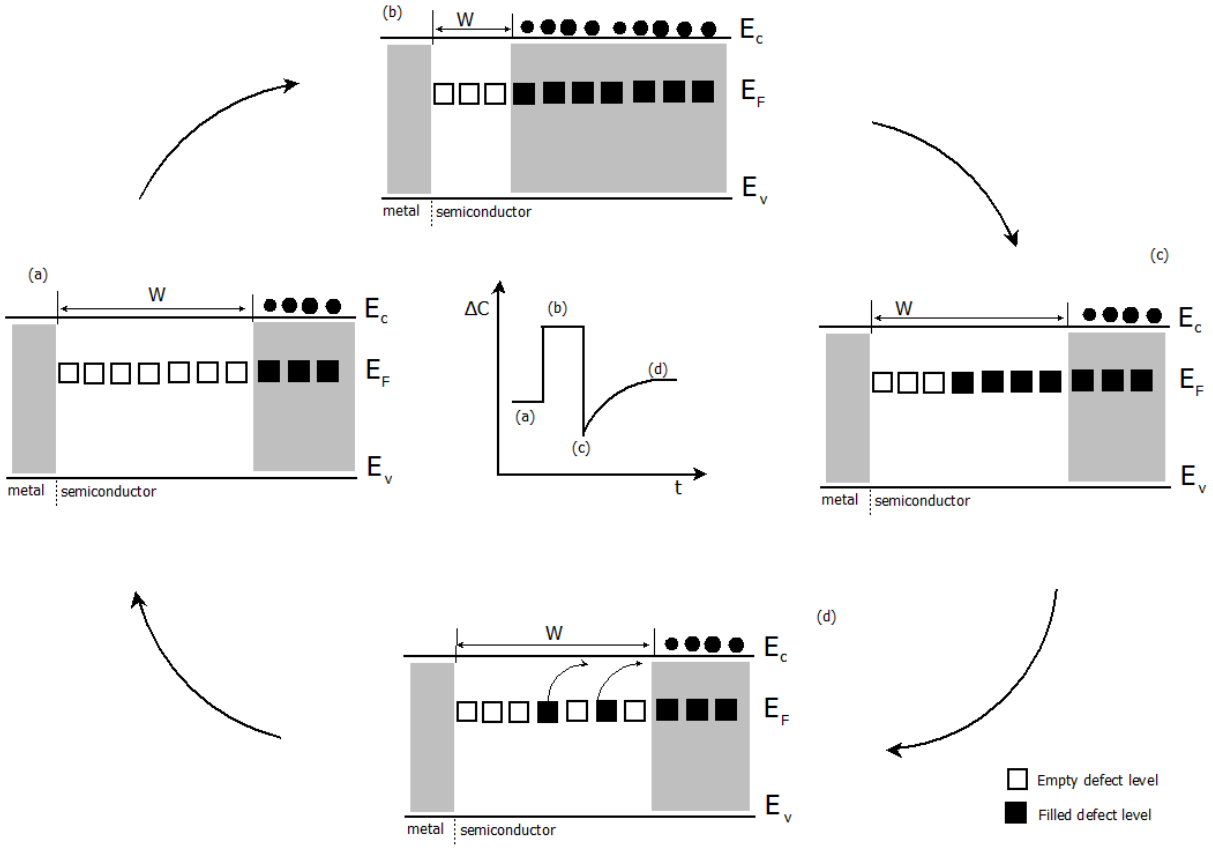

Fig. 4.2: Variation of the depletion width and trap concertation in response to voltage biasing conditions for an electron trap in an n-type semiconductor. (a) diode reverse biased, (b) during a filling pulse, (c) directly after pulse removal and (d) a time t after pulse removal. The capacitance transient during the cycle is shown at the centre of the figure.

From the time dependence of the capacitance transient, the electron emission rate is determined, during experiments. The density of the occupied traps at time t after removing the filling pulse is given by [58],

$$N(t) = N_T exp(-e_n t) \qquad (4.35)$$

where N_T is the trap concentration assuming all the traps were initial filled and e_n is the thermal emission rate. For $N_T \ll N_D$, the junction capacitance can be expressed as a time dependent function given by [59],

$$C(t) = C_o - \Delta C_o \, exp(-e_n t) \qquad (4.36)$$

where $C_o$is the equilibrium reverse bias voltage capacitance and ΔC_o is the change in capacitance observed immediately after removing the pulse.

4.4.1 The DLTS concept

The conventional DLTS is a highly sensitive capacitance or current measurement technique with a good transient response and is capable of resolving signals due to different traps from each other. Amongst other features and the ones mentioned above, the DLTS principle of operation lies in the processing of capacitance transient obtained after a repeated pulsing sequence. During temperature scanning, since the thermal emission process is strongly dependent on the temperature, the peak position of the observed spectra shift to higher temperatures for high emission rates and to lower temperatures for lower emission rates. This allows for a unique determination of the peak position by using a rate window thermal scan [35].

Initially, DLTS used a dual-gate average for a precise determination of the emission rate window and for signal averaging, enhancing the signal to noise ratio. This averaging helps in detection of lower concentration traps. Considering the fact that there is no lower limit on the rate window, it is ideal to work with rate windows above $1s^{-1}$. Due to the thermal scan time is long, so below $1s^{-1}$ rate window, performing signal averaging would require an exceptionally long time [13]. Fig. 4.3 illustrate how a double boxcar technique is used to select a rate window.

Fig. 4.3.a, shows a transient signal produced from the double boxcar with pre-set times t_1 and t_2. The average difference between the capacitance at t_1 and t_2 are plotted as function of temperature as shown on Fig. 4.3.b. The values of t_1 and t_2 determine the rate window of DLTS thermal scan. The capacitance difference changes as a function of temperature as indicated in Fig. 4.3.b. It increases until it reaches a maximum (peak) and then it starts decreasing on either side of the peak. The peak is formed only when the decay constant τ falls within the order of $t_2 - t_1$.

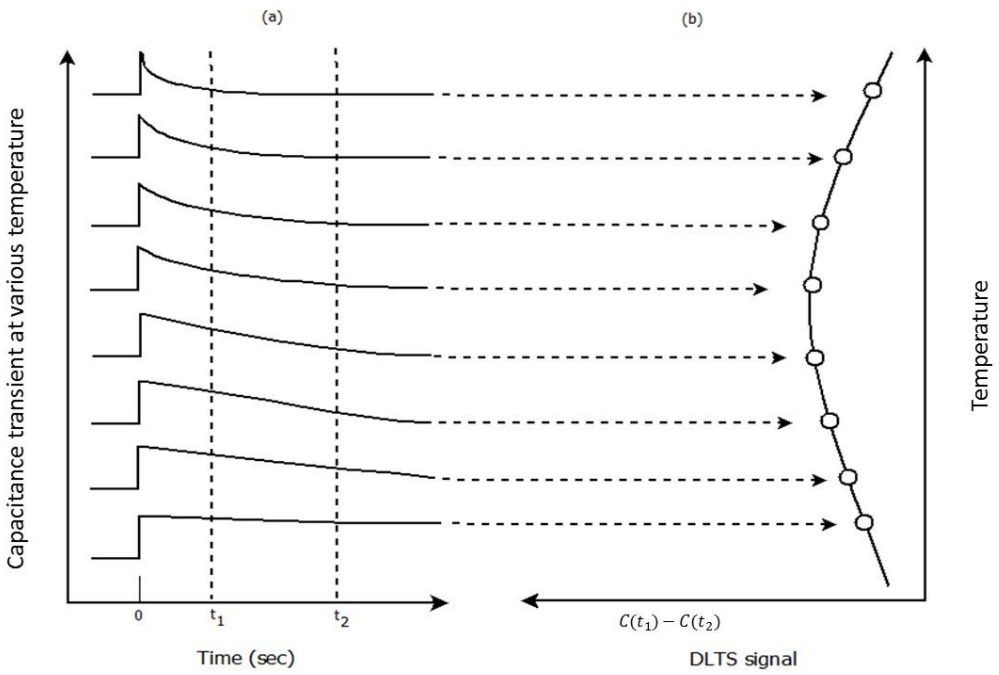

Fig. 4.3: The change in the shape of a DLTS transient with increasing temperature (a) and the DLTS signal obtained from the transients as a function of sample temperature (b).

The value of τ at the maximum of the $C(t_2) - C(t_1)$ versus temperature for a particular trap, τ_{max} can be related to gate positions t_1 andt_2. This is achieved by normalizing the DLTS signal given by

$$S(T) = [C(t_1) - C(t_2)]/\Delta C(0) \qquad (4.37)$$

where $\Delta C(0)$ is the capacitance due to the pulse change at $t = 0$. For exponential transients,

$$S(T) = [exp(-t_1/\tau)] - [exp(-t_2/\tau)] \qquad (4.38)$$

this can be rewritten as,

$$S(T) = exp(-t_1/\tau)\,[1 - exp(-\Delta t/\tau)] \qquad (4.39)$$

where $\Delta t = t_2 - t_1$. Thus the relationship between τ_{max}, t_1 and t_2 can be obtained by differentiating $S(T)$ with respect to τ and equating the results to zero:

$$\tau_{max} = \frac{t_1 - t_2}{ln(t_1/t_2)} \qquad (4.40)$$

The emission rate of a peak on a DLTS spectra obtained from a thermal scan can be precisely and uniquely determined. Performing a thermal scan with many different rate windows enables one to identify the peak positions and the temperatures at which they occur.

4.4.2 Defect depth profiling

The DLTS technique can be employed in the determination of the spatial distribution of a defect within a given semiconductor and thus help in the prediction of the defect introduction rate. Assuming that the DLTS signal peak height is directly proportional to the concentration of a deep level, the concentration can be obtained directly from a capacitance change observed using a complete trap filling pulse width. The concentration of the defect under this concept is given by [59],

$$N_T = \frac{2\Delta C(0)}{C} N_d \qquad (4.41)$$

where $\Delta C(0)$ is the capacitance change just after removing the complete trap filling pulse, C is the junction capacitance under quiescent reverse bias conditions and N_d is the net doping concentration obtained using the *CV* profiling technique. The concentration of the defect is usually underestimated when using Eq. 4.41, particularly for thin films and under low reverse bias conditions. For an accurate estimation of the trap concentration, consider the region λ in Fig. 4.1 where the trap level crosses the Fermi level at a distance λ shallower than the depletion region edge. In this region, the trap is filled and does not contribute to the capacitance transient when a filling pulse has been applied. The width of the transition region is given by [13]

$$\lambda = \left[\frac{2\varepsilon(E_F - E_T)}{q^2 N_D}\right]^{1/2} \qquad (4.42)$$

where ε is the semiconductor dielectric constant, q is the electronic charge. In order to determine the defect distribution profile, the defect states within the region to be profiled must be filled. The variation of the trap concentration with depth can be obtained using the fixed bias-variable pulse method. This method monitors the incremental change in capacitance $\delta(\Delta C)$ with a small change in the majority carriers filling pulse height, δV_p. The relative increment change in capacitance due to the pulse increment can be expressed by [59]

$$\delta\left(\frac{\Delta C}{C}\right) = \left(\frac{\varepsilon}{qw^2 N_D}\right)\frac{N_T(x)}{N_D(x)}\delta V_p \qquad (4.43)$$

where x is the depth below the junction, N_D is the ionized shallow impurity concentration, w is the depletion region width, corresponding to quiescent reverse bias conditions. $N_D(x)$ is obtained from C-V measurements. Double integration of the Poisson Eq. based on the detailed derivation by Zohta and Watanabe [59], gives the total signal due to a majority

carrier pulse. The corrected expression for the concentration of the deep level defect is given by [8],

$$N_T = \frac{2\Delta C(0) N_{D(x)}}{C}\left[\left(\frac{x-\lambda}{x}\right)^2 - \left(\frac{x_p-\lambda_p}{x}\right)^2\right]^{-1} \qquad (4.44)$$

where $x-\lambda$ and $x_p-\lambda_p$ are the depletion widths before and after applying a filling pulse width, respectively. λ_p is the distance from the depletion region edge to the point where the trap levels crosses the Fermi level during the application of the pulse, under low noise measurements, defect concentration of the order of $10^{10}\text{cm}^{-3}$are detectable.

Chapter 5

Experimental Techniques

5.1 Introduction

In the formation of metal-semiconductor contacts, the handling/preparation of the samples plays an important role. As for the characterization techniques discussed in the previous chapter, different techniques can be employed in the preparation of contacts, such as cleaning and metal deposition. In this chapter, detailed explanations of the experimental techniques are outlined.

5.2 Sample preparation

In this study, undoped ZnO single crystal samples from Cermet Inc. were used. Prior to the fabrication of the Schottky and ohmic contacts, the samples were degreased in acetone, then methanol both for five minutes in an ultrasonic bath. The five minutes degreasing in methanol was followed by three minutes boiling in hydrogen peroxide at a temperature of 100 ^{o}C. After treatment with hydrogen peroxide, the samples were blown dry with nitrogen gas, immediately followed by contact fabrication.

5.3 Contact fabrication

Ohmic contacts with composition of Al/Au and relative thicknesses of 50/30 nm were deposited on the Zn polar face using the resistive evaporation technique at a pressure of approximately 1 x 10^{-6} torr. Palladium Schottky contacts of diameter 0.6 mm and thickness of 60 nm were fabricated on the O-polar face of the ZnO samples using the resistive evaporation system under a vacuum of approximately 1 x 10^{-6} torr as shown in Fig. 5.1.

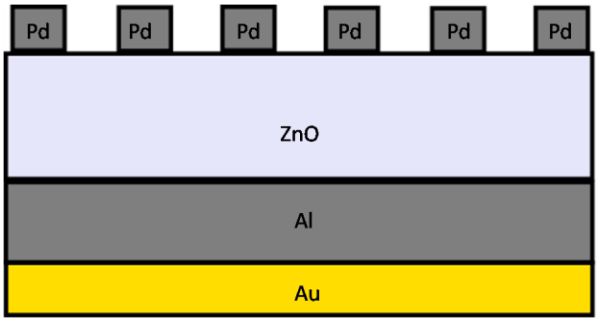

Fig. 5.1: Schematic diagram of metal-ZnO Schottky and ohmic contact.

5.4 Sample annealing

A Lindberg annealing furnace was used for all the required annealing. In semiconductors, annealing of the crystals can at times introduce or remove defects. The furnace can anneal from lower temperatures to a maximum of 1200 ℃. Different ambient condition such as air, oxygen, nitrogen and argon can be connected to the furnace depending on the type of the atmosphere or ambient required. Different annealing tubes and sample holders were used for a specific material to minimize contaminants on the surface. The samples in this study were annealed in Argon for 30 minutes at 800 ℃ before contact fabrication.

5.5 Current-Voltage and Capacitance-Voltage measurements

Electrical characterization through *IV* and *CV* measurements were carried out in dark closed station to ensure there was no interference from light. A DC voltage source 4140B and Hewlett Packard pA meter, which can measure from 10^{-15}A with accuracy of 0.5% was used. From the *IV* measurements, numerous parameters were deduced such as Schottky barrier height, ideality factor, saturation current, series resistance, forward and reverse leakage currents. Whereas in *CV* measurements an HP 4192A LF impedance analyser, which can measure from 5 Hz to 13 MHz frequency range. Also several parameters can be extracted from the *CV* measurements such as SBH and free carrier concentration [35].

Furthermore, temperature dependent *IV* measurements were performed. The samples were attached to gold plated ceramic plates after bonding of thin gold wires on the Schottky contacts using silver paints. The silver paint was used for ohmic contacts as well. An automated program written in Labview^{tm} was used to perform temperature depended *IV* measurements were performed in a closed cycle helium cryostat in the 30-350 K temperature range [14]. Values of SBH, ideality factor, series resistance, saturation current and generation recombination current were obtained from the curves. The transport mechanism were determined from the nature of the curves.

5.6 Deep Level Transient Spectroscopy (DLTS) and Laplace-DLTS

In this study, conventional DLTS and high resolution Laplace DLTS were used to characterize the defects in ZnO. A schematic diagram of the DLTS and Laplace-DLTS system is depicted in Fig. 5.2.

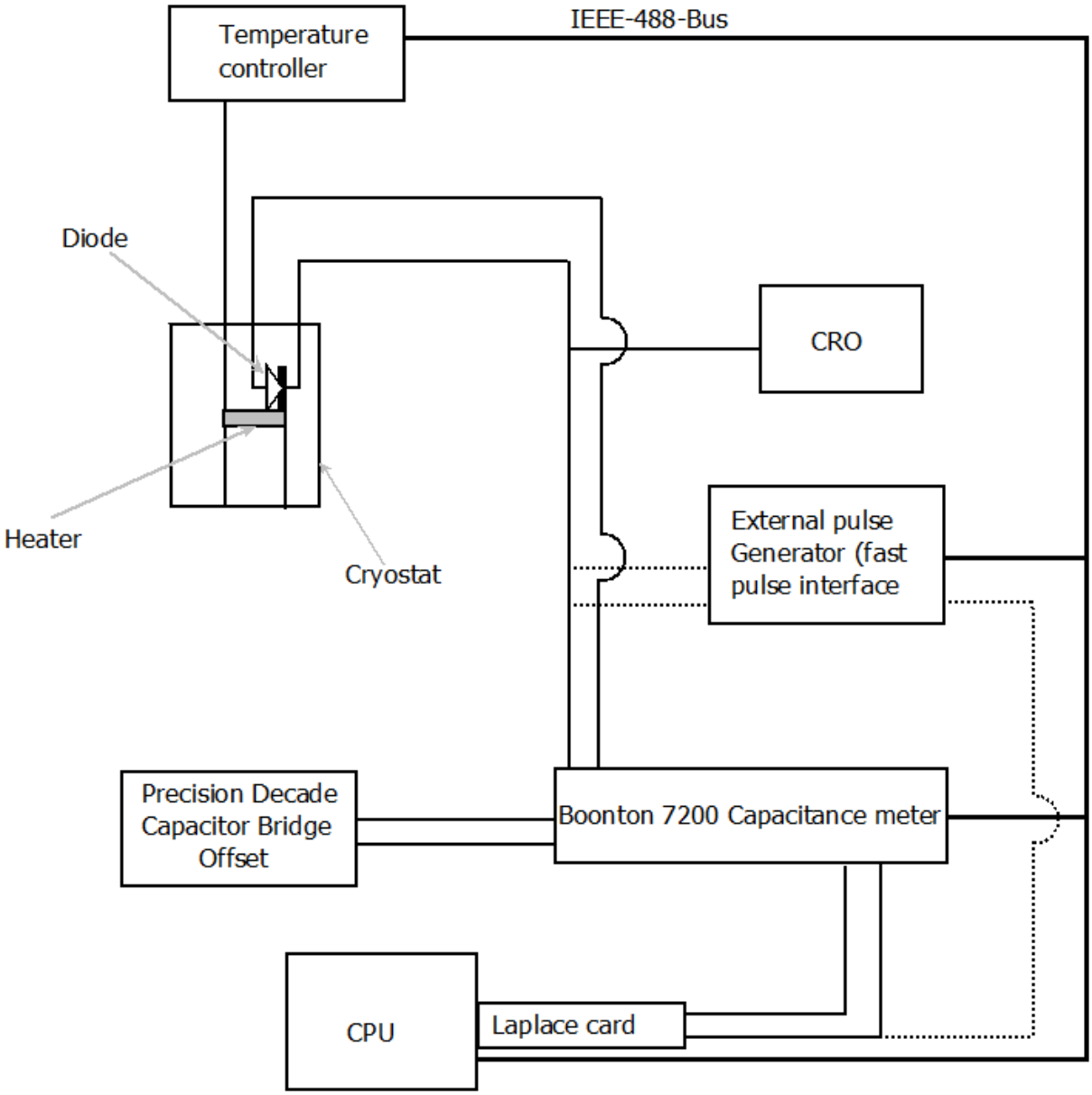

Fig. 5.2: Schematic diagram of the DLTS and Laplace- DLTS system. The dotted lines shows the necessary connections when an external generator is used.

In the system, the sample is mounted in a closed cycle helium cryostat. A Lakeshore 340 temperature controller is used to monitor the temperature in the range of 16 – 380 K. Thermal emission of the carriers after excitation by the pulse generator was monitored by Boonton 7200 capacitance meter with a 100 mV and 1 MHz AC voltage signal. The software and Laplace card with an internal pulse generator for generating the desired quiescent bias voltage and pulses, it also has a data collection and processing system. These are used to analyse and average transients before displaying the spectra for both the DLTS and Laplace-DLTS [59]. The Laplace card is also used to record the capacitance-temperature scans. The Laplace card has difficulties in producing well-defined signals for short filling pulse widths.

Hence, the need for an external signal generator with a fast pulse interface for measurements that require the use of pulses with shorter filling pulse widths.

The Laplace program sets up sample excitation parameters for both conventional DLTS and Laplace-DLTS. The parameters include measurement initiation, capacitance transient acquisition conditions and conversion into a DLTS or Laplace-DLTS spectrum. In conventional DLTS mode, the capacitance meter measures the capacitance transients after excitation and is processed by the Laplace card. The DLTS spectrum is determined by the use of a particular rate window with temperature ramping up or down. In case of Laplace-DLTS mode, the capacitance meter also monitors the capacitance transient after excitation at a fixed temperature. The Laplace card performs transient averaging and implements the inverse Laplace transform to calculate the signal magnitude and emission rate using different routines: CONTIN, FTIKREG and FLOG before a Laplace spectrum is displayed [11].

5.7 Alpha-particle irradiation

The Schottky barrier diodes were bombarded at room temperature with 1.6 MeV alpha-particles in the Van de Graaff accelerator. During the bombardment, the dose rate was 1.8 x 10^{+11} alpha-particles $cm^{-2}s^{-1}$ and the dose incremented in steps of 2.5 x 10^{+13} up to 5 x 10^{+14} cm^{-2}. After each increment inside the same chamber capacitance-temperature scan at zero reverse bias in the 20-350 K temperature range. The defects introduced during the irradiation were characterized by conventional DLTS.

Chapter 6

Results and Discussion

6.1 Temperature-dependent *IV* measurements on ZnO Schottky barrier diodes

6.1.1 Introduction

Analysis of *IV* characteristics of Schottky barrier diodes only at room temperature, provide insufficient information about the transport mechanism or the formation of a barrier at the metal-semiconductor interface, since under different temperature conditions there are different transport mechanisms, which dominate. A detailed outline of parameters extracted from temperature-dependent *IV* measurements will be discussed in this section.

6.1.2 Results and discussion

In Fig. 6.1 shows the semi-logarithmic current-voltage plot of Pd/ZnO Schottky barrier diodes in the 100-300 K temperature range. The *IV* curves show a strong dependence on temperature. It can be clearly observed that the characteristics of the device deviate from ideality at low temperatures. Such deviations are attributed to the effect of other current transport mechanisms other than thermionic emission (TE), which included the generation-recombination of the carriers in the space charge region and tunnelling of electrons through the barrier [14]. At temperatures above 200 K, TE becomes the dominant current transport mechanism.

Fig. 6.2 shows a plot of the barrier height and the ideality factor as a function of temperature. The ideality factor decreases with an increase in temperature. The high values at lower temperature can be attributed to the change in the current transport process from generation-recombination and other transport mechanisms. The observed increase in barrier height with increase in temperature disagrees with the negative coefficient of II-VI semiconductor materials [8]. Several researchers [48, 56, 60], have observed the same trend on various Schottky contacts and explained it to be possibly related to the temperature activated current transport of carriers across the metal semiconductor interface

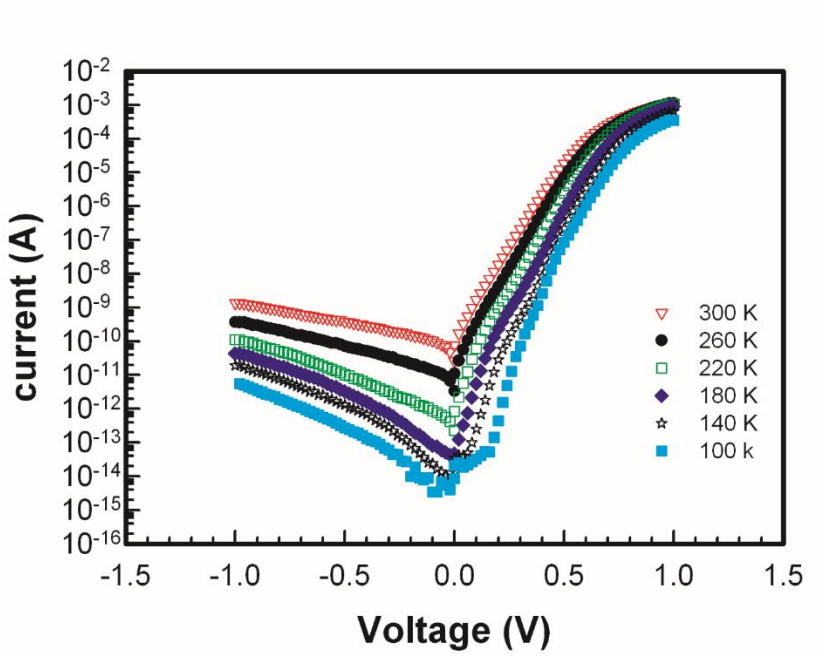

Fig. 6.1: Temperature dependent current-voltage semi-logarithmic plot for Pd/ZnO Schottky barrier diodes in the 100-300 K temperature range.

These carriers at low temperatures are able to tunneling through the lower barriers and therefore the current will be dominated by transport of the charge carriers through the patches of lower SBH. As the temperature increase, many electrons gain sufficient energy to surmount the barrier height areas through TE.

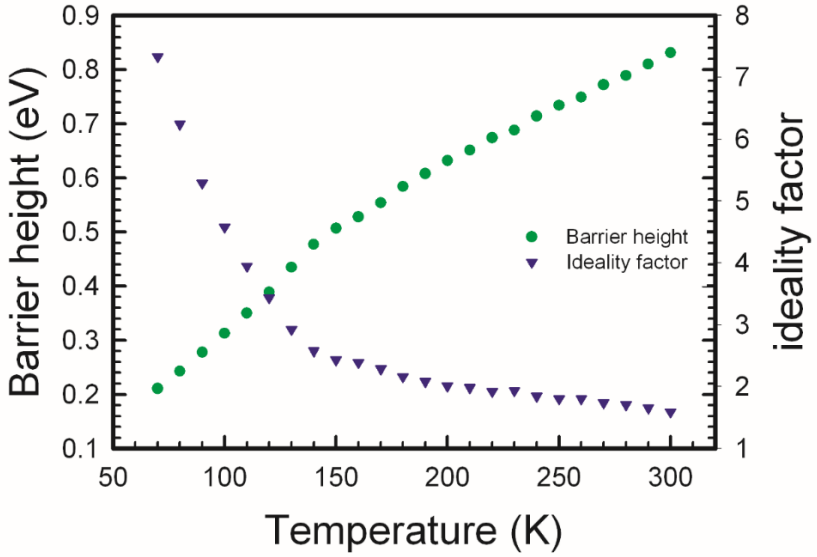

Fig. 6.2: Barrier height and ideality factor as a function of temperature for Pd/ZnO -Schottky barrier diodes.

The Richardson constant can also be determine from the intercept of the $ln(I_s/T^2)$ vs. 1000/T plot presented in Fig. 6.3. The plot shows two linear regions (140-200 and 210-300 K) and a deviation is observed in the temperature range below 200 K. The Richardson constant in the 140-200 K region is 3 × 10^{-12} ^{9}A cm^{-2} K^{-2} and 3 × 10^{-9}A cm^{-2} K^{-2} in the 210-300 K temperature range. These values are much lower compared to the theoretical value of 32 A cm^{-2} K^{-2} in n-type ZnO. The deviation in the Richardson plot may be due to the presence of the spatially inhomogeneous barrier height and the potential fluctuations at the interface that consist of low and high barrier areas i.e. when the temperature is lowered, the current will flow preferentially through the lower barriers in the potential distribution [14].

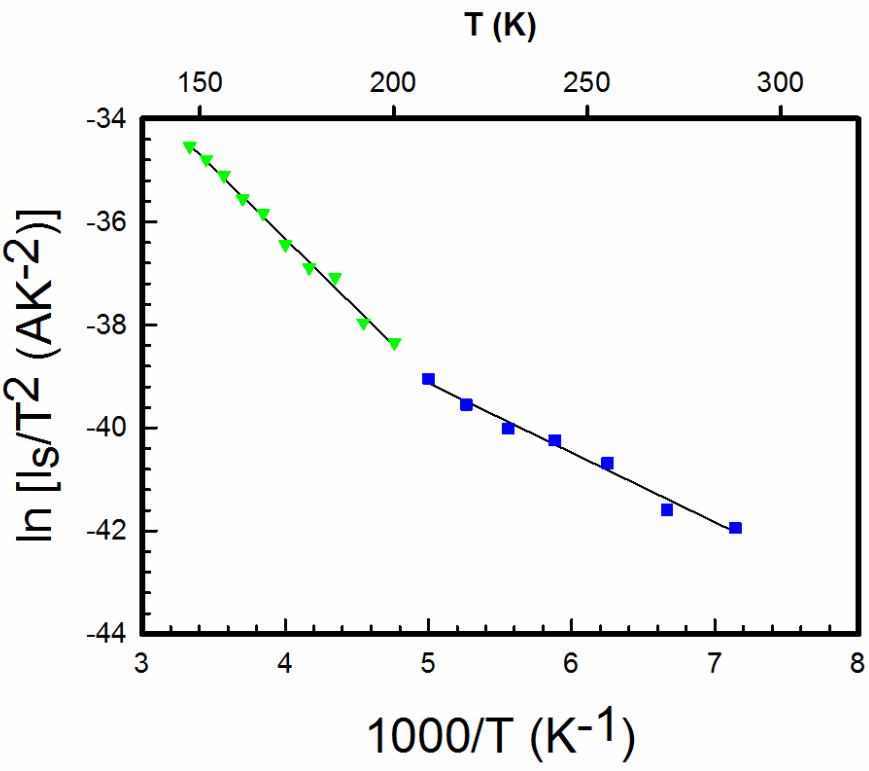

Fig. 6.3: Richardson plot, ln (I_s/T^2) versus 1000/T, for the Pd/ZnO SDB in the 140-30OK temperature range.

As indicated in Fig. 6.3, the saturation current plot has shown non-linearity at lower temperatures. To address these observed irregularities, one can correct the barrier height inhomogeneities accord to the Gaussian distribution of the barrier height. Fig. 6.4 shows a modified Richardson plot using the experimental data of the saturation current. The modified Richardson constant were calculated to be 39 and 39 A cm^{-2} K^{-2} in the 140-200 and 210-300 K temperature ranges, respectively. These values are in a close agreement with the theoretical value of 32 A cm^{-2} K^{-2}. The difference in the calculated values of the Richardson constant for different temperature ranges can be attributed to inhomogeneity in the barrier. These findings

shows how *IV* characteristics can be model using the TE model at high temperatures indicating that the TE is the dominant transport mechanism, while at lower temperatures the abnormal behaviours can be attributed to current flow through the low Schottky barrier areas and tunneling.

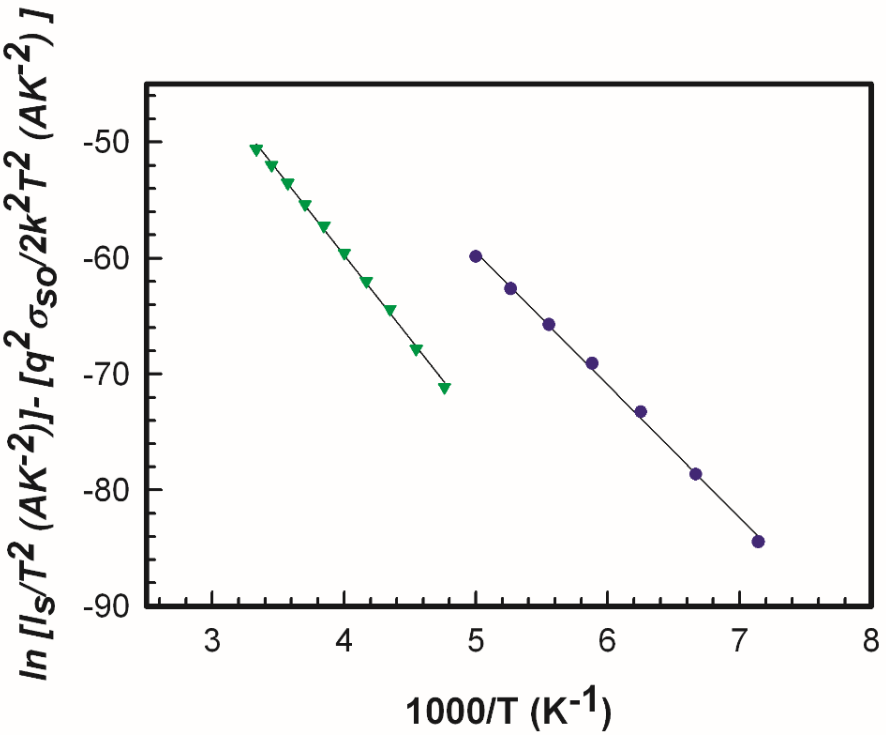

Fig. 6.4: Modified Richardson plot for the Pd/ZnO Schottky diode according to the Gaussian distribution of the barrier heights.

From figure 6.1 the forward bias current voltage (*I-V*) characteristics are linear on the semi-logarithmic scale from 0.5 V and greater and then bend due to series resistance (R_s). Hence, it is of vital importance to determine the R_s using a variety of methods. The simplest way to determine the$R_s$values is Ohm's law, which yields R_s as dV/dI in the forward bias region. Another way of determining the R_s is by Cheung &Cheung's method in order to compare with Ohm's law [60-63]. The forward bias *I-V* characteristics due to TE theory of Schottky diodes with the R_s can be expressed as Cheung's functions [64]:

$$\frac{dV}{d(\ln I)} = IR_s + n\left(\frac{kT}{q}\right) \qquad (6.1)$$

and

$$H(I) = V - n\left(\frac{kT}{q}\right) ln\left(\frac{I}{AA*T^2}\right) = n\Phi_{bo} + IR_s \qquad (6.2)$$

From figure 6.5(a), the plot is linear with R_s as the gradient and $n\Phi_{bo}$ as the y-axis intercepts derived from Eq. 6.1. The insert in figure 6.5(a) shows a plot of the whole range of the forward bias *I-V* data, which can be divided into two regions. In region I, the ideality factor is similar to that obtained using ohm's law, with high values of R_s, where the R_s determined from region II are in good agreement with those of obtained from the *I-V* curves. The observed behaviour can be attributed to the existence of the R_s, interface states and to the voltage drop across the interfacial layers. Furthermore, the plot of H(I)-I is linear, with the gradient of this plot providing a different determination of R_s.Thus, by using the value of the n obtained from Eq. 6.2 the value of Φ_{bo}can be calculated from the y-axis intercept of the H(I)-*I* plot. The plot of H(I)-I is shown in figure 6.5(b), in the 80-320 K temperature range. Similar observations were reported by Durmus et al [65] on Au/n-Si SBD and Kinaci at al [66] on Au/TiO_2/*n*-Si SDB.

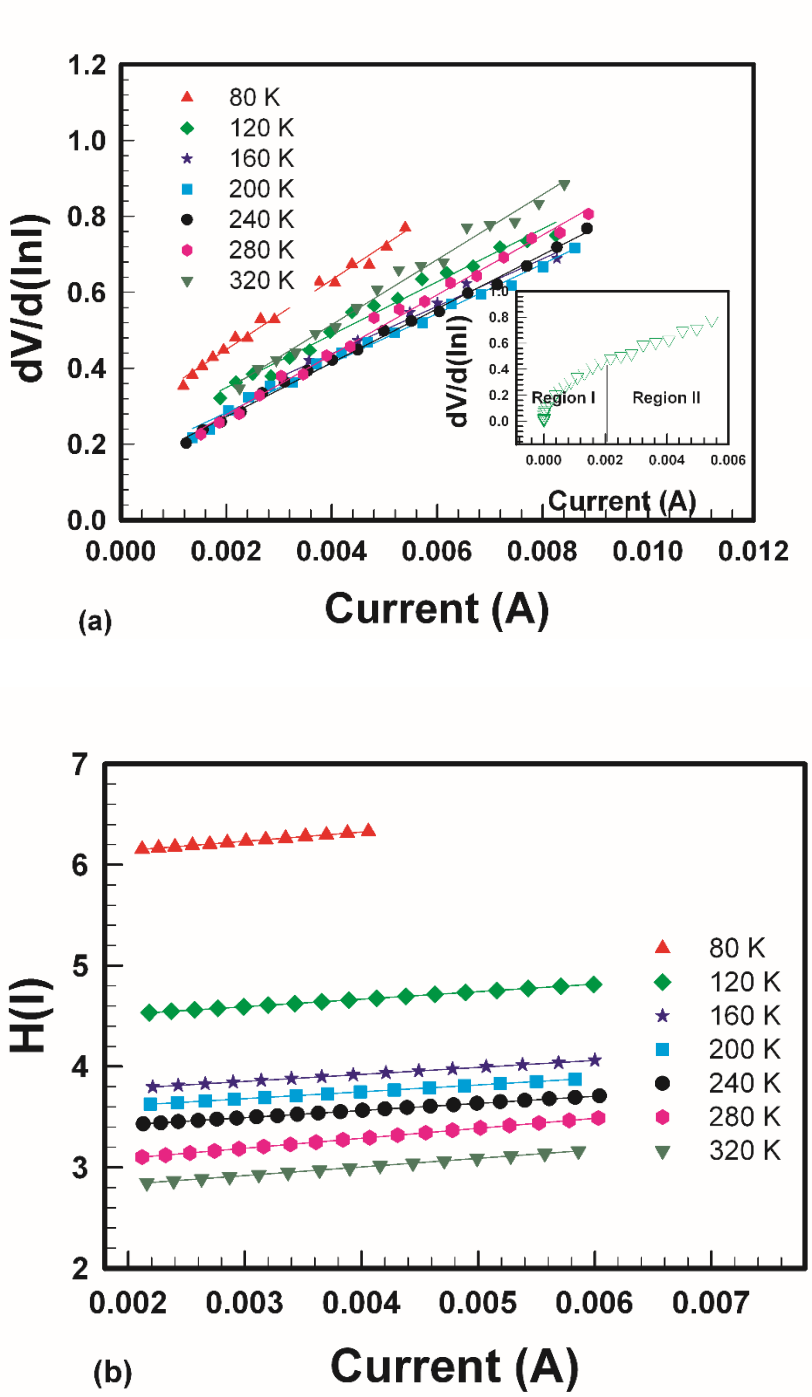

Fig.6.5: (a) and (b) Cheung and Cheung against the forward current characteristics of Pd/ZnO Schottky barrier diodes.

The R_s obtained from the three different techniques were plotted in Fig. 6.6 as a function of temperature. Mtangi *et al* [67] showed a similar trend of series resistance obtained from *ln I-V* plots on Pd/ZnO SBD in the 60-300 K temperature range. They explained the observed trend to be related to bulk resistivity of the sample determined from the Hall effect

measurements, where a transition in the conductivity occurs near 180 K. From Fig. 6.6 shows that at lower temperatures (60-180 K), the R_s decreases with increase in temperatures, while showing an absolute minimum near 180 K and increases with temperature at high temperatures (T > 200 K).

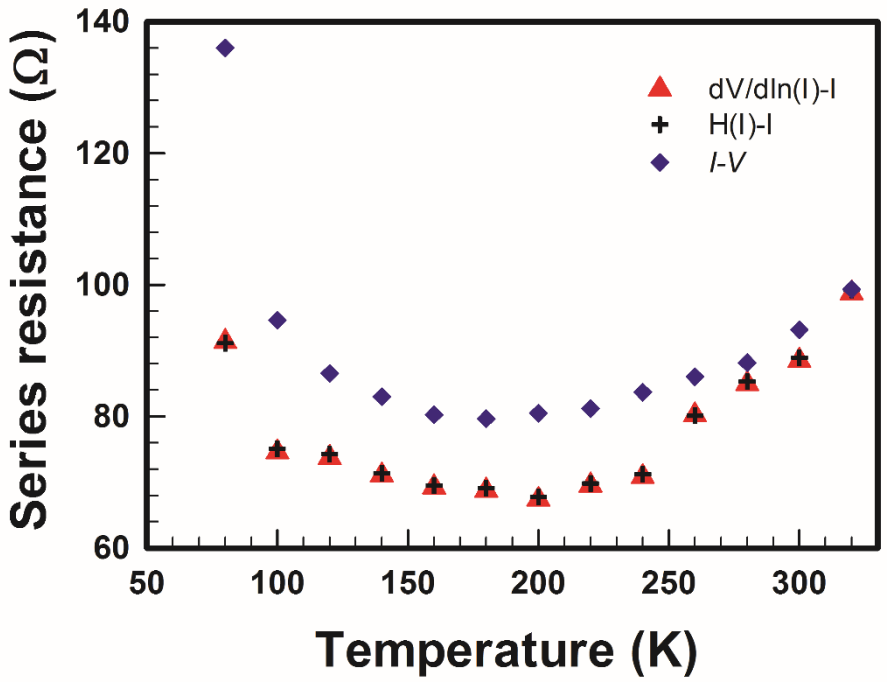

Fig.6.6: Series resistance as a function of temperature determined using three different methods.

6.1.3 Conclusion

We investigated the *IV* characteristics of Pd/ZnO SBDs in the 30-300 K temperature range. The series resistance obtained in this study are in good agreement with literature and with each other. The current transport mechanism at lower temperature is dominated by the current flow through the low Schottky barrier areas and tunneling. Meanwhile at high temperatures TE is the dominant current transport mechanism. From the temperature dependence of *IV* measurements, the barrier height was observed to increase with increase in temperature and the ideality factor decrease with increasing temperature. These is attributed to the existence of barrier height inhomogeneity. Such inhomogeneities have been successfully explained based on the TE model with the assumption of Gaussian distribution of the barrier height.

A detailed analysis of temperature dependent current voltage characterization is given in the attached publications.

6.2 Irradiation induced defects

6.2.1 Introduction

ZnO has a direct bandgap of 3.4 eV, which plays a role in realizing blue and ultraviolet light emitting devices, such as lasers, light emitting diodes and daylight-blind UV detectors, as is the case for GaN with a similar bandgap [8, 33]. In addition, the large bandgap enables ZnO suitable for the fabrication of catalysts, solar cells and as a substrate for the group III-nitride based devices. For space applications, these devices have to operate at elevated temperatures, approximately above 200 ℃, in harsh conditions comprising of energetic particles [17]. In this section, we report on the electrical characterization of high-energy alpha-particles bombarded single crystal ZnO.

6.3.2 Results and discussion

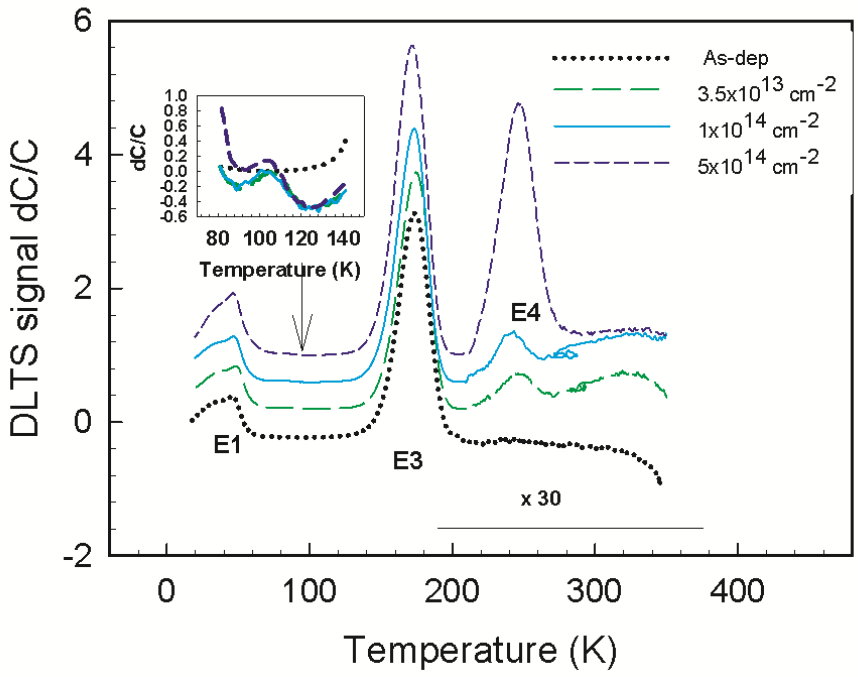

Fig. 6.7: DLTS spectra of as-deposited and after α-particle irradiated with 1.6 MeV Pd/ZnO Schottky barrier diodes. All spectra were recorded using a quiescent reverse bias 2V, a filling pulse amplitude of 2.2V and filling pulse width of 0.2 ms. The insert shows the E2 defect. The amplitude of the E4 defect was multiplied by 30.

Fig. 6.7 shows DLTS spectra of as-deposited Pd/ZnO SBDs and after 1.6 MeV $\boldsymbol{\alpha}$-particle irradiation. The spectra shows two prominent peaks that have also been observed in the as-grown ZnO samples. The defects (E1 & E3) are common defects in ZnO regardless of the growth, processing and contact fabrication techniques [32, 67]. After the samples were bombarded with 1.6 MeV $\boldsymbol{\alpha}$-particles, two other defects (E2 & E4) appeared. E2 has been reported in literature and it does not appear in all ZnO materials. It also appears to increase in magnitude with an increase α-particle dosage. However, the E4 has been observed to be introduced by annealing and high-energetic particle irradiations [3, 32]. The Arrhenius plots used to determine the activation enthalpy and apparent capture cross-section of the E1, E2, E3 and E4 deep level defects are shown in Fig. 6.8.

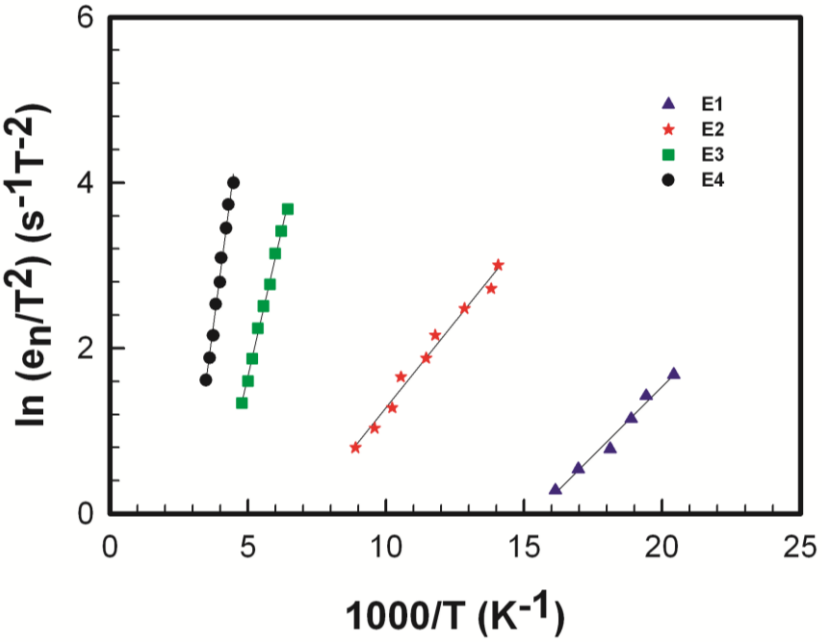

Fig. 6.8: Arrhenius plot obtained from the 1.6 MeV alpha-particle irradiated Schottky barrier diodes.

From the DLTS spectrum in Fig. 6.7, the E1 peak is asymmetric. This could be attributed to the fact that it is observed very close to the freeze out region. The capacitance-temperature scan showing the freeze out region of ZnO is shown in Fig. 6.9.

Fig. 6.9 shows a variation of capacitance with temperature for the as-deposited and after α-particle irradiation on ZnO samples. From these scans, it can be concluded that the freeze-out for ZnO begins around 50 K, where the capacitance drops sharply with decrease in temperature. The position of the E1 peak near the freeze out region can influence the accurate determination of its activation enthalpy and capture cross-section. Values of estimated

activation enthalpies, capture cross-sections in relation with irradiation energies are shown in Table 6.1.

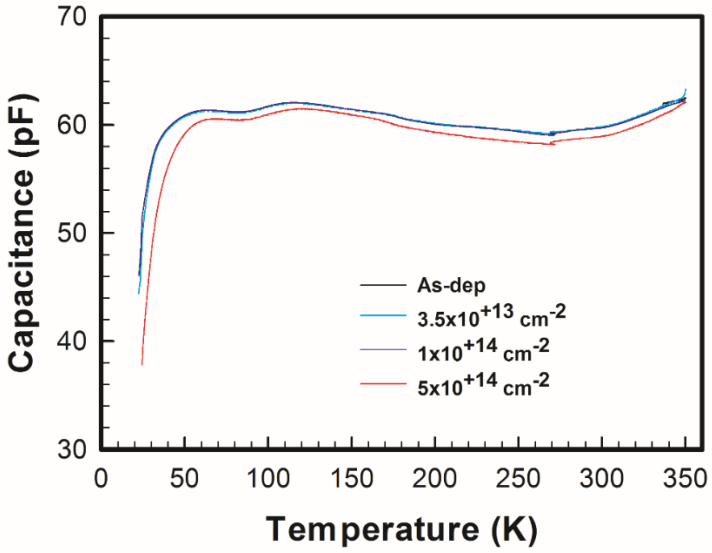

Fig. 6.9: Capacitance-temperature scan obtained as-deposited and after α-particle irradiated with 1.6 MeV on Pd/ZnO Schottky barrier diodes. The spectra were recorded at quiescent reverse bias of 0V in the 20-350 K temperature range.

Based on the summary presented in Table 6.1, it can be clearly observed that the activation enthalpy is influenced by the irradiation dosages as well as the capture cross-sections. Thus, the identities of the native defects in ZnO are not clear yet. However, the only valid conclusion is that ZnO contains the E1 and E3 defects independent of the technique used for the material growth.

Table 6.1: Electronic properties of prominent defects detected by DLTS in as-deposited and after irradiation with 1.6 MeV α-particle on Pd/ZnO SBDs.

Irradiation energy (MeV)	E1		E2		E3		E4	
	E_T (meV)	σ_a (cm^2)	E_T (meV)	σ_a (cm^2)	E_T (meV)	σ_a (cm^2)	E_T (meV)	σ_a (cm^2)
As-deposited	115	2.6×10^{-13}	____	_____	290	1.1×10^{-15}	_____	_____
$3.5 \times 10^{+13}$ cm^{-2}	72	8.5×10^{-16}	86	$3. \times 10^{-18}$	304	2.3×10^{-15}	518	9.2×10^{-14}
$1 \times 10^{+14}$ cm^{-2}	66	2.4×10^{-17}	78	1.3×10^{-18}	288	2.9×10^{-16}	514	1.9×10^{-14}
$5 \times 10^{+14}$ cm^{-2}	55	4.1×10^{-17}	87	4.1×10^{-18}	289	1.1×10^{-15}	526	1.1×10^{-13}

6.3.3 Conclusion

Exposing ZnO to α-particles introduces additional deep level defect. The defects concentrations indicate that ZnO is highly resistant to radiation damage to some extent. The irradiation induced peak has proven to be stable for the dosage of particles bombarded in this particular study. Part of these results have been submitted as paper to SAIP 2015.

Chapter 7

Conclusions

Electrical characterization of ZnO has been successfully achieved by different techniques. The current transport mechanisms and the quality of Schottky diodes were characterized using current-voltage (*IV*) measurements. In addition, the electrical characterization of process and irradiation induced defects in ZnO have been successfully achieved using conventional and Laplace DLTS techniques. Conclusions drawn from these studies are given at each section in chapter 6. In this chapter, the majority highlights of the study are briefly stated.

ZnO Schottky contacts revealed a strong dependence on temperature. Closer to room temperature and higher, the current transport mechanisms has proved to be predominately thermionic emission, while at low temperatures, the contacts have shown the dominance of other mechanisms such as generation-recombination or tunneling, other than pure thermionic emission. The barrier heights on the Schottky contacts were measured using the *IV* and *CV* techniques. From the *IV* measurements, the barrier height has proven to be affected by barrier inhomogeneities leading to a trend in which the Schottky barrier height increases with an increase in temperature, a trend that disagrees with the negative temperature coefficient of the II-VI compound semiconductor material.

As-grown single crystal ZnO samples contain two prominent (E1 & E3) deep level defects. These defects are common in ZnO, despite different ways of growth, processing and contact fabrication techniques. High-energetic particle irradiation introduced additional defects (E2 & E4) in ZnO. The E2 and E4 have low concentrations that indicate that ZnO is highly resistant to radiation damage to some extent. The irradiation-induced peaks have proven to be stable for the exposed dosage on the samples.

Publication 1: Temperature-dependent current-voltage characteristic of Pd/ZnO Schottky barrier diodes and the determination of the Richardson constant

Materials Science in Semiconductor Processing 34 (2015) 359–364

Contents lists available at ScienceDirect

Materials Science in Semiconductor Processing

journal homepage: www.elsevier.com/locate/mssp

Temperature-dependent current–voltage characteristics of Pd/ZnO Schottky barrier diodes and the determination of the Richardson constant

Meehleketo A. Mayimele, Mmantsae Diale *, Wilbert Mtangi, Francois D. Auret

Physics department, University of Pretoria, Pretoria 0002, South Africa

ARTICLE INFO

Available online 13 March 2015

Keywords:
I–V characteristics
Temperature-dependent
Richardson constant
Barrier Inhomogeneities
Gaussian Distribution

ABSTRACT

We report on a systematic investigation of temperature dependent current–voltage (*I–V*) characteristics of Pd/ZnO Schottky barrier diodes in the 30–300 K temperature range. The ideality factor was observed to decrease with increase in temperature, whilst the barrier height increases with increase in temperature. The observed trend has been attributed to barrier inhomogeneities, which results in a distribution of barrier heights at the interface. Using the dependence of saturation current values on temperature, we have calculated the Richardson constant (A^*) which was investigated in the two distinct temperature regions: 140–200 K and 210–300 K and values of 3×10^{-12} and 3×10^{-9} A cm^{-2} K^{-2} were obtained, respectively. A mean barrier height of 0.97 eV was obtained in the 140–300 K temperature range. Applying the barrier height inhomogeneities correction, the value of A^* was obtained from the modified Richardson plots as 39.43 and 39.03 A cm^{-2} K^{-2} in the 140–200 K and 210–300 K temperature range. The modified Richardson constant (A^{**}) has proved to be strongly affected by barrier inhomogeneities and dependent on contact quality.

1. Introduction

Zinc Oxide (ZnO) has gained a lot of global interest in the research community because of its direct and wide band gap of 3.37 eV. It has a larger exciton binding energy of 60 meV and hence a high efficiency in excitonic emission [1,2]. In addition, it has superior electronic properties such as high breakdown voltage, high electron saturation velocity, high thermal conductivity and is very resistant to high-energy radiation, making it a very suitable candidate for applications in space and around nuclear reactors [3,4]. Furthermore, ZnO has found applications in a number of semiconductor electronic devices such as ultraviolet and blue-range optoelectronics, lasers, photovoltaics, field effect transistors, microwave diodes and sensors [5]. Another attractive characteristic of ZnO is its amenability to conventional wet chemistry etching, being compatible with silicon technology. The ease of etching ZnO with all acids and alkalis offers an opportunity for the fabrication of small-size devices [4,6]. In realizing semiconductor-based devices, high quality Schottky contacts are critical. The fabrication of semiconductor-based devices is of vital importance as it determines the use of the material in both electronic and opto-electronic applications [4]. The fabrication of high quality devices is influenced by several factors, some of which include, but not limited to semiconductor surface contaminants, metal-surface chemical reaction and subsurface defects [1,7,8]. These factors can in turn influence the current–voltage characteristics of devices such as current transport mechanisms.

A good understanding of current transport mechanisms is required for a complete explanation of the current transport across a metal–semiconductor (MS) contact. Several

* Corresponding author. Tel.: +27 124204418.
E-mail address: mmantsae.diale@up.ac.za (M. Diale).

http://dx.doi.org/10.1016/j.mssp.2015.02.018
1369-8001/

researchers have studied current transport properties of Schottky contacts at room temperature in which a thermionic emission (TE) model has been used to calculate the diode parameters [9,10]. In these calculations, it was assumed that TE is the dominant current transport mechanism. However, it has been noted and reported that the analysis of the electrical characteristics of the Schottky barrier diodes (SBDs) only at room temperature does not give sufficient information about the conduction process or the barrier formation at the MS interface [9,11,12]. In cases where current–voltage measurements were performed at other temperatures other than room temperature, it has been demonstrated that TE is not the only transport mechanism [13–16]. An assumption that TE is the only mechanism responsible for the transport of charge carriers across the MS interface could result in erroneous values of the diode parameters. Since transport mechanisms varies in different temperature ranges, there is a need to perform further analysis on the temperature-dependence of *I–V* measurements to comprehensively describe the current transport mechanisms and obtain accurate values of the diode parameters at different temperatures.

Several researchers [1,5,17–19] have investigated the temperature-dependence of the *I–V* characteristics of metal/ZnO Schottky diodes and determine several diode parameters in different temperature regions. Asil et al. [19] investigated the temperature dependence of current–voltage characteristics on electro-deposited p-ZnO/n-Si heterojunctions. The authors reported a mean barrier height of 0.818 eV in the 160–300 K temperature range. Gür et al. [2] studied high temperature Schottky diode characteristics of bulk ZnO and reported a mean barrier height of 0.74 eV in the 240–400 K temperature range. Mtangi et al. [20] investigated the temperature dependence of Pd/ZnO SBDs and reported a mean barrier height of 0.50 eV in the 180–300 K temperature range. Kim et al. [17] investigated the temperature-dependence of Ag Schottky contacts to differently grown O-polar bulk ZnO. From their *I–V* characteristics, the authors revealed a mean barrier height of 0.701 eV in the 200–300 K temperature range. Furthermore, Von Wenchstern et al. [21] investigated the temperature dependence of the *I–V* characteristics on Pd Schottky contacts on ZnO thin films and reported a mean barrier height of 1.16 ± 0.04 eV in the 200–290 K temperature range. Since the researchers obtained different values of barrier heights in different temperature ranges, this shows that the barrier height is strongly dependent on temperature and hence the need to conduct further studies on temperature-dependence of *I–V* measurements in order to determine the accurate values of barrier heights in different temperature regimes.

Since the determination of the barrier height involves the use of the Richardson constant A^*, there is also a need to know the exact value of the Richardson constant for the temperature range in which the barrier height is being evaluated. Several reports have revealed a variation of A^*, where different values have been obtained or calculated in different temperature regions [2,17,20,22,23] as indicated in table 1. These deviations have been explained by assuming the presence of the barrier height inhomogeneities, where two different approaches were used in defining the inhomogeneities. One approach, assumes a continuous spatial distribution of the Schottky barrier height (SBH) and the total current cross a Schottky diode is simply calculated by integrating the current determined by the ideal TE theory with an individual barrier height and weighted by the distribution function. In another approach, it is assumed that some small patches of low SBH are embedded in the uniform SBH area.

Table 1
Richardson constants determined in different temperature ranges.

	Richardson Constant ($A\,cm^{-2}\,K^{-2}$)	Temparature range (K)	Authors
1	0.272	300–420	[26]
2	0.248	240–440	[2]
3	10	293–423	[39]
4	19.54	300–423	[22]
5	46.3	100–300	[17]
6	123	210–300	[23]
7	167	80–180	[20]

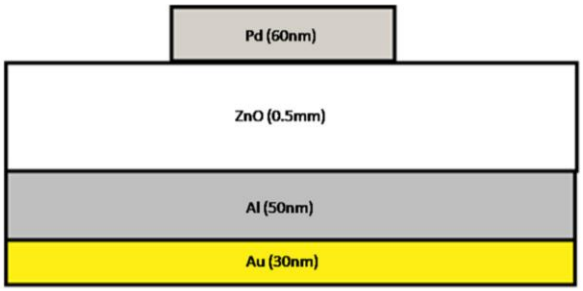

Fig. 1. Schematic diagram of Pd/ZnO/Al/Au SBD.

The deviation from the TE model observed in the *I–V* characteristics could be quantitatively explained by the TE mechanism with a Gaussian distribution of the Barrier heights [24]. Hence, we investigated temperature-dependent *I–V* measurements on Pd/ZnO SBD in the 30–300 K temperature range and determined the Richardson constant that is closer to the theoretical value n-ZnO using the modified plot.

2. Experiment

In this study, we used bulk single crystals of undoped ZnO samples from Cermet Inc. [25]. Prior to the fabrication of the Schottky and Ohmic contacts, the samples were degreased in acetone, then methanol for five minutes in an ultrasonic bath. The five minutes degreasing in methanol was followed by three minutes boiling in hydrogen peroxide at a temperature of 100 °C. After treatment with hydrogen peroxide, the samples were blown dry with nitrogen gas. Ohmic contacts with composition of Al/Au and relative thicknesses of 50/30 nm as shown in Fig. 1, were deposited on the Zn polar face using the resistive evaporation technique at a pressure of approximately 1×10^{-6} Torr. Palladium Schottky contacts of diameter 0.6 mm and thickness of 60 nm were fabricated on the O-polar face of the ZnO samples using the resistive evaporation system under a vacuum of approximately 1×10^{-6} Torr. Temperature-dependent *I–V* measurements were performed in a closed cycle Helium cryostat in the 30–300 K temperature range.

3. Results and discussion

Fig. 2, shows the semi-logarithmic plot of *I–V* characteristics of Pd/ZnO obtained in the 80–300 K temperature range. The curves obtained from Fig. 2, show a very strong temperature dependence of the Pd/ZnO Schottky barrier diodes. It can be clearly observed that the characteristics of the device deviate from ideality at low temperatures (30–140 K). Such deviations are usually attributed to the effect of other current transport mechanisms, which include the generation-recombination of the carriers in the space charge region and tunneling of electrons through the barrier [20]. At temperatures above 200 K, thermionic emission becomes the dominant current transport mechanism [1,26]. From Fig. 2, the experimental values of ideality factor (n) and the barrier height (Φ_{ap}) were determined using the intercepts and the gradients of the forward bias *I–V* characteristics at each temperature, respectively by fitting the pure thermionic emission model to the experimental data.

Using the pure thermionic emission model, the current through a uniform metal–semiconductor interface can be expressed as [27]

$$I = I_s \exp\left[\frac{q(V-IR_s)}{nkT}\right]\left\{1-\exp\left(\frac{q(V-IR_s)}{kT}\right)\right\} \quad (1)$$

where R_s is the series resistance, q is the electron charge, V is the forward-bias voltage, k is the Boltzmann constant, T is the absolute temperature, n is the ideality factor and I_s is the saturation current derived from the straight-line intercept of the $\ln I$ versus V i.e. at $(V=0V)$ and is defined by

$$I_s = AA^*T^2\exp\left(-\frac{q\phi_{ap}}{kT}\right) \quad (2)$$

Where A is the effective diode area, A^* is the effective Richardson constant, Φ_{ap} is the apparent zero-bias barrier height. The ideality factor (n) in Eq. (1) can be obtained as [28]

$$n = \frac{q}{kT}\left(\frac{dV}{d\ln I}\right) \quad (3)$$

The zero-bias barrier height $\Phi_{Bo}(I–V)$ is determined from the saturation current I_s, obtained at $V=0\,V$ and is given by

$$\phi_{Bo} = \frac{kT}{q}\ln\left[\frac{AA^*T^2}{I_s}\right] \quad (4)$$

Fig. 3 shows a plot of barrier height Φ_{ap} and the ideality factor as a function of temperature. The zero-bias barrier height values have been calculated from Eq. (2) by assuming pure thermionic emission of charge carriers across the barrier. The ideality factor decreases with increase in temperatures. The obtained high values at lower temperature can be attributed to the change in the current transport process from generation recombination and other transport mechanisms. A similar trend were also observed by several authors [3,17,19,20]. The observed increase in barrier height with increase in temperature disagrees with the negative temperature coefficient of II–IV semiconductor material [29,30]. Several researchers have observed the same trend on various Schottky contacts [12,27,30,31] and they have explained it to be possibly related to the temperature-activated current transport of carriers across the MS interface. These carriers at low temperatures are able to surmount the lower barriers through tunneling and therefore the current will be dominated by transport of charge carriers through the patches of lower SBH. As the temperature increases, many electrons gain sufficient energy to surmount the higher barrier areas through thermionic emission [3,4]. As a result, the obtained barrier height will increase with increase in temperature and bias voltage.

3.1. Richardson constant

To obtain the mean barrier height and the Richardson constant in a range of temperatures, Eq. (2), can be linearized as [32]

$$\ln\left(\frac{I_s}{T^2}\right) = \ln(AA^*) - \frac{q\Phi_{Bo}}{kT} \quad (5)$$

The Richardson constant can also be determined from the intercept of the $\ln(I_s/T^2)$ versus $10^3/T$ plot shown on Fig. 4. The plot shows some linear behavior at high temperatures (140–200 and 210–300 K) and a deviation from linearity is observed in the temperature range below 140 K. The non-linearity of the conventional energy $\ln(I_s/T^2)$ versus $10^3/T$

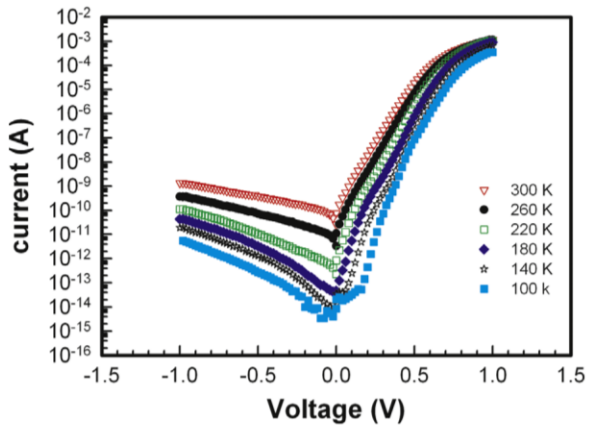

Fig. 2. Temperature dependent *I–V* semi logarithmic plot for the as-deposited Pd/ZnO SBD in the 80–300 K temperature range.

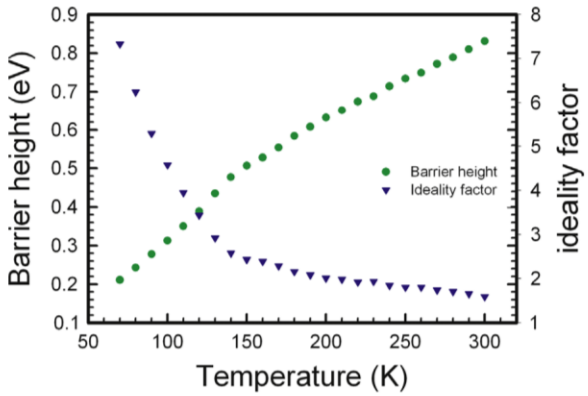

Fig. 3. Barrier height and ideality factor as a function of temperature in the 80–300 K temperature range for Pd/ZnO SBD.

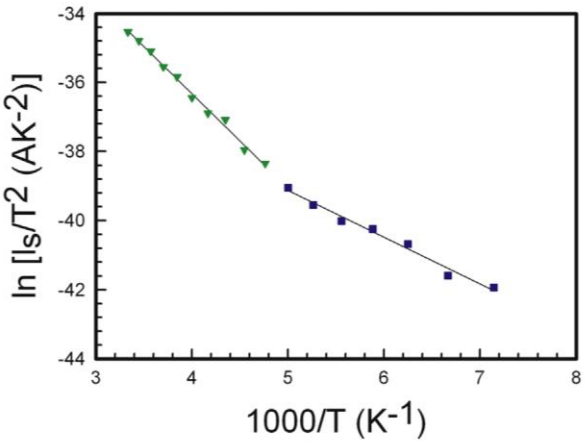

Fig. 4. Richardson plot, $\ln(I_s/T^2)$ versus 1000/T, for the Pd/ZnO SDB in the 80–300 K temperature range.

plot is caused by the dependence of the barrier height and the ideality factor on temperature reported by several researchers [9,14,31,33]. Two distinct regions have been identified where linear plots could be fitted to the experimental data. From these two regions, the Richardson constant values are 3×10^{-12} and 3×10^{-9} A cm^{-2} K^{-2} in the 140–200 K and 210–300 K temperature ranges, respectively. These values are much lower compared to the theoretical value of 32 A cm^{-2}K^{-2} in n-ZnO. An effective barrier height of 0.11 and 0.24 eV has been calculated in the 140–200 K and 210–300 K temperature range. The deviation in the Richardson plot may be due to the presence of the spatially inhomogeneous barrier height and the potential fluctuations at the interface that consists of low and high barrier areas, i.e. when the temperature is lowered, the current will flow preferentially through the lower barriers in the potential distribution [9,12,14,20,31].

3.2. Barrier height inhomogeneities

In addressing the observed inhomogeneities in the Schottky barrier diodes, which deviates from classical TE theory, some researchers have considered a system of discrete regions of low barrier areas imbedded in a high background of uniform barrier [34–36]. These behaviors can be explained by assuming the Gaussian distribution of the barrier heights with a mean value Φ_b and standard deviation σ_s, which can be given by [37]

$$P(\Phi_b)=\frac{1}{\sigma_s\sqrt{2\pi}}\exp\left[-\frac{(\Phi_b)-\overline{\Phi}_b}{2\sigma_s^2}\right] \tag{6}$$

where $1/\sigma_s\sqrt{2\pi}$ is the normalization constant of the Gaussian barrier height distribution. The total $I(V)$ across a Schottky diode containing a barrier inhomogeneities can be expressed as [34]

$$I(V)=\int_{-\infty}^{+\infty} I(\Phi_b,V)P(\Phi_b)d\phi_b \tag{7}$$

where $I(\Phi_b,V)$ is the current at a bias V for a barrier height based on the ideal thermionic emission-diffusion (TED) theory and $P(\Phi_b)$ is the normalization distribution function giving the probability of accuracy for the barrier height [38]. Substituting Eq. (1) for $I(\Phi_b,V)$ and Eq. (6) for $P(\Phi_b)$ in Eq. (7), we obtain the current $I(V)$ through the Schottky barrier at a forward bias V but with a modified barrier as [34]

$$I(V)=I_s\exp\left(\frac{qV}{n_{ap}kT}\right)\times\left[1-\exp\left(-\frac{qv}{kT}\right)\right] \tag{8}$$

with

$$I_s=AA^*T^2\exp\left(-\frac{q\Phi_{ap}}{kT}\right) \tag{9}$$

where n_{ap} and Φ_{ap} are the apparent ideality factor and apparent barrier height at zero bias, respectively, given by [24,28],

$$\Phi_{ap}=\Phi_b(T=0)-\frac{q\sigma_{so}^2}{2kT} \tag{10}$$

and

$$\left(\frac{1}{n_{ap}}-1\right)=\rho_2-\frac{q\rho_3}{2kT} \tag{11}$$

It is assumed that the mean SBH, Φ_b and the standard deviation, σ_s are linearly bias-dependent on Gaussian parameters, such that $\overline{\Phi}_b=\overline{\Phi}_{bo}+\rho_2V$ and a standard deviation $\sigma_s=\sigma_{so}+\rho_3V$, where $\overline{\Phi}_{bo}$ is the barrier height at temperature $T=0$ K, ρ_2 and ρ_3 are voltage coefficients which may depend on temperature, quantifying the voltage deformation of the barrier height distribution [20]. The temperature dependence of σ_s is small and therefore can be neglected. The decrease of zero-bias barrier height is caused by the existence of a Gaussian distribution and the extent of influence is determined by the standard deviation itself [20,34].

The current transport of electrons across a Schottky barrier is affected by the presence of barrier inhomogeneities. These are attributed to fact that charge carriers have insufficient energy to surmount the barriers at low temperatures. Thereby, at these temperature ranges tunneling becomes the dominant transport mechanism of electrons. The tunneling of the electrons through low barrier areas will cause a deviation of the barrier height from the actual value obtained for a homogeneous barrier at the metal–semiconductor interface. A linear fit for the apparent ideality factor, which obeys Eq. (10) has been obtained and shown in Fig. 5. In the low

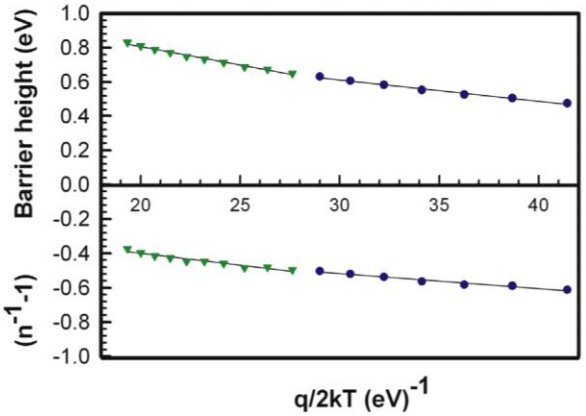

Fig. 5. Zero-bias apparent barrier height and ideality factor versus $q/2kT$ curves of the Pd/ZnO SBD according to the Gaussian distribution of the barrier heights.

temperature region, the decrease in Φ_{Bo} is caused by the existence of the Gaussian distribution and the extent of influence is determined by the standard deviation itself. In addition, the effect is particularly significant at low temperatures [20]. The fitting of the experimental data using Eqs. (2) or (9) and in Eq. (3) gives Φ_{ap} and n_{ap} at zero bias, respectively, which should obey Eqs. (10) and (11). Thus, the plot of Φ_{ap} versus $q/2kT$ (Fig. 5) should be a straight line that gives Φ_{bo} and σ_{so} from the intercepts and the slope, respectively. From Fig. 4, the values of Φ_{bo} are 0.986 and 1.234 eV in the 140–200 K and 210–300 K temperature ranges. Von Wenchstrern et al. [21] obtained similar results. The values of σ_{so} are 109 and144 mV in the 140–200 K and 210–300 K temperature ranges, respectively. The lower the value of the σ_{so}, the more homogeneous the barrier height is and the better the diode rectifying performance [20]. The temperature dependence of the ideality factor can be understood based on Eq. (11). Fig. 5, shows a linear fit of the ideality factor where the voltage coefficients ρ_2 and ρ_3 are obtained from the intercept and slope, respectively. From Fig. 5, $\rho_2 = -256$ and -123 mV and $\rho_3 = -8.7$ and -13.9 mV in the 140–200 K and 210–300 K temperature ranges, respectively. The linear behavior of the plot shows that the ideality factor expresses the voltage deformation of the Gaussian distribution of the SBD.

3.3. The modified Richardson plot

As indicated in Fig. 3, the saturation current plot, $\ln(I_s/T^2)$ versus $10^3/T$ has shown non-linearity at low temperatures. To address these observed irregularities, one can correct for the barrier height inhomogeneities according to the Gaussian distribution of the barrier height and can therefore modify Eq. (5) to give [24,35]

$$I_s = AA^{**}T^2 \exp\left[-\frac{q\Phi_{ap}}{kT} + \frac{q^2\sigma_{so}^2}{2k^2T^2}\right] \tag{12}$$

and

$$\ln\left(\frac{I_s}{T^2}\right) - \left(\frac{q^2\sigma_{so}^2}{2k^2T^2}\right) = \ln(AA^{**}) - \frac{q\Phi_{ap}}{kT} \tag{13}$$

Fig. 6, shows a modified Richardson plot, using the experimental I_s data. A modified $\ln\left(I_s/T^2\right) - (q^2\sigma_{so}^2/2k^2T^2)$ versus $10^3/T$ plot according to Eq. (13) should give a straight line with a slope directly yielding the mean barrier height and the intercept $\ln(AA^{**})$ relating to the modified Richardson constant A^{**} for a given diode area A. The two values of σ_{so} were calculated from Fig. 5, in the 140–200 K and 210–300 K temperature ranges. From the straight line of the modified saturation current plots, the mean zero-bias barrier heights were obtained as 0.98 and 1.24 eV in the 140–200 K and 210–300 K temperature ranges, respectively. The intercepts give A^{**} as 39.44 and 39.03 A cm^{-2} K^{-2} in the 140–200 and 210–300 K temperature ranges, respectively. These values are in a close agreement with the theoretical value of 32 A cm^{-2} K^{-2} compared to those reported in Table 1, by several researchers [2,17,20,22,23]. The difference in the calculated values of the Richardson constant for different temperature ranges can be attributed to inhomogeneity in the barrier. These findings shows how I–V characteristics can be modeled using the TE model at high temperatures indicating that TE is the dominant transport mechanism, while at low temperatures, the abnormal behaviors can be attributed to current flow through the low Schottky barrier areas and tunneling.

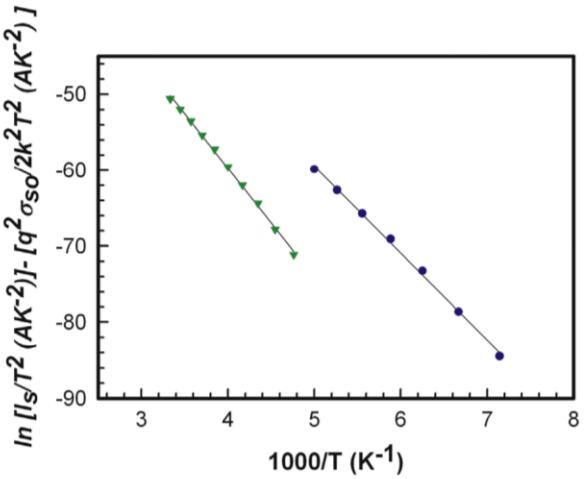

Fig. 6. Modified Richardson plot for the Pd/ZnO SBD according to the Gaussian distribution of the barrier heights.

4. Conclusion

We have investigated the I–V characteristics of Pd/ZnO SBDs in the 30–300 K temperature range. From the temperature dependence of I–V measurements, the BH was observed to increase with increasing temperature and ideality factor decreases with increasing temperature. The observed variation of the barrier height with temperature disagrees with the negative temperature coefficient of II–VI compound semiconductor materials. Apparent Richardson constant, A^* values were obtained as 3.03×10^{-12} and 3.28×10^{-9} A cm^{-2} K^{-2} in the 140–200 K and 210–300 K temperature range, respectively. The values of A^* has showed a strong dependence on the metal–semiconductor contact quality and saturation current. After the barrier height inhomogeneities correction, the modified Richardson constant, A^{**} obtained from the modified Richardson plot, was 39.44 and 39.03 A cm^{-2} K^{-2} in the 140–200 K and 210–300 K temperature range, respectively. The modified Richardson constant obtained in the modified plot is closer to the theoretical value for n-ZnO. The mean barrier height was evaluated to be 0.98 eV in the 140–200 K. The value of A^{**} proved to be strongly affected by barrier inhomogeneities and dependent on contact quality. At high temperatures (210–300 K), the I–V characteristics can be modeled using the thermionic emission model, an indication that thermionic emission is the dominant current transport mechanism, while at low temperatures, the abnormal behaviors in the I–V curves can be attributed to current flow through the low Schottky barrier areas and tunneling.

Acknowledgment

This work has been made successful through the financial support of the South African National Research Foundation (NRF) and the University of Pretoria (Grant number 88021).

References

[1] S.M. Faraz, V. Khranovskyy, R. Yakimova, A. Ulyashin, Q. Wahab, in: Proceedings of the 2011 IEEE Regional Symposium on, Micro and Nanoelectronics (RSM), 2011, pp. 48–51.
[2] E. Gür, S. Tüzemen, B. Kiliç, C. Coşkun, J. Phys. Condens. Matter 19 (2007) 196–206.
[3] W. Mtangi, F.D. Auret, C. Nyamhere, P. Janse van Rensburg, A. Chawanda, M. Diale, J.M. Nel, W.E. Meyer, Phys. B: Condens. Matter 404 (2009) 4402–4405.
[4] Ü. Özgür, Y.I. Alivov, C. Liu, A. Teke, M.A. Reshchikov, S. Doğan, V. Avrutin, S.-J. Cho, H. Morkoç, J. Appl. Phys. 98 (2005) 041–301.
[5] H.L. Mosbacker, Y.M. Strzhemechny, B.D. White, P.E. Smith, D.C. Look, D.C. Reynolds, C.W. Litton, L.J. Brillson, Appl. Phys. Lett. 87 (2005) 012–102.
[6] D.J. Rogers, F. Hosseini Teherani, A. Ougazzaden, S. Gautier, L. Divay, A. Lusson, O. Durand, F. Wyczisk, G. Garry, T. Monteiro, M.R. Correira, M. Peres, A. Neves, D. McGrouther, J.N. Chapman, M. Razeghi, Appl. Phys. Lett. 91 (2007) 071–120.
[7] W. Mtangi, J.M. Nel, F.D. Auret, A. Chawanda, M. Diale, C. Nyamhere, Phys. B: Condens. Matter 407 (2012) 1624–1627.
[8] M. Allen, M. Alkaisi, S. Durbin, Appl. Phys. Lett. 89 (2006) 103520-1–103520-3.
[9] I. Afandiyeva, S. Demirezen, Ş. Altındal, J. Alloy. Compd. 552 (2013) 423–429.
[10] I. Hussain, M.Y. Soomro, N. Bano, O. Nur, M. Willander, J. Appl. Phys. 112 (2012) 064–506.
[11] M. Asghar, K. Mahmood, M. Faisal, M. Hasan, J. Phys. Conf. Ser. 439 (2013) 012–030.
[12] A. Özdemir, A. Turut, A. Kökçe, Semicond. Sci. Technol. 21 (2006) 298.
[13] A.J. Mathai, C.K. Sumesh, B.P. Modi, Phys. Semicond. Devices (2011) 85–87.
[14] H. Korkut, N. Yildirim, A. Turut, Microelectron. Eng. 86 (2009) 111–116.
[15] S.S. Naik, V.R. Reddy, Adv. Mater. Lett. 3 (2012) 188–196.
[16] D.S. Reddy, M.B. Reddy, N.N.K. Reddy, V.R. Reddy, J. Mod. Phys. 2 (2011) 113–123.
[17] H. Kim, A. Sohn, Y. Cho, D.-W. Kim, J. Electron. Packag. 135 (2013) 011010.
[18] I. Hussain, M. Soomro, N. Bano, O. Nur, M. Willander, J. Appl. Phys. 113 (2013) 234–509.
[19] H. Asil, K. Çinar, E. Gür, C. Coşkun, S. Tüzemen, Int. J. Phys. Sci. 8 (2013) 371–379.
[20] W. Mtangi, F.D. Auret, C. Nyamhere, P.J. Janse van Rensburg, A. C.M.D., Phys. B: Condens. Matter 404 (2009) 1092–1096.
[21] H. von Wenckstern, G. Biehne, R.A. Rahman, H. Hochmuth, M. Lorenz, M. Grundmann, Appl. Phys. Lett. 88 (2006) 092–102.
[22] D. Somvanshi, S. Jit, IEEE Electron Device Lett. 34 (2013) 1238–1240.
[23] S. Ranwa, P. Kumar Kulriya, V. Dixit, M. Kumar, J. Appl. Phys. (2014) 233706.
[24] S. Chand, J. Kumar, Appl. Phys. A 63 (1996) 171–178.
[25] ⟨http://www.cermetinc.com/materials/n__ZnO_substrate_product_lit(2014)⟩.
[26] R. Yatskiv, J. Grym, App. Phys. Lett. 101 (2012) 3928–3933.
[27] D. Korucu, S. Duman, Thin Solid Films 531 (2013) 436–441.
[28] A. Gümüş, A. Türüt, N. Yalçin, J. Appl. Phys. 91 (2002) 245–250.
[29] B.G. Yacobi, Semiconductor Materials: An Introduction to Basic Principles, Springer, US, 2013.
[30] E. Özavcı, S. Demirezen, U. Aydemir, A.Ş. Sens, Actuators A: Phys. 194 (2013) 259–268.
[31] H. Tecimer, A. Türüt, H. Uslu, Ş. Altındal, İ. Uslu, Sens. Actuators A: Phys. 199 (2013) 194–201.
[32] J.H. Werner, H.H. Güttler, J. Appl. Phys. 69 (1991) 1522–1533.
[33] D. Korucu, S. Duman, Thin Solid Films 531 (2013) 436–441.
[34] İ. Dökme, Ş. Altindal, M.M. Bülbül, Appl. Surf. Sci. 252 (2006) 7749–7754.
[35] Y. Song, R. Van Meirhaeghe, W. Laflere, F. Cardon, Solid-State Electron. 29 (1986) 633–638.
[36] S. Chand, J. Kumar, Appl. Phys. A 63 (1996) 171–178.
[37] N. Bannov, V. Aristov, V. Mitin, R.E. Schmitsdorf, T.U. Kampen, W. Monch, R.F. Schmitsdorf, Surf. Sci. 324 (1995) 249–256.
[38] S. Chand, J. Kumar, J. Appl. Phys. 82 (1997) 5005–5010.
[39] M.W. Allen, X. Weng, J.M. Redwing, K. Sarpatwari, S.E. Mohney, H. von Wenckstern, M. Grundmann, S.M. Durbin, Electron Devices IEEE Trans. 56 (2009) 2160–2164.

Publication 2: Analysis of temperature-dependent current-voltage characteristic and extraction series resistance in Pd/ZnO Schottky barrier diodes

Physica B 480 (2016) 58–62

Contents lists available at ScienceDirect

Physica B

journal homepage: www.elsevier.com/locate/physb

Analysis of temperature-dependant current–voltage characteristics and extraction of series resistance in Pd/ZnO Schottky barrier diodes

M A Mayimele*, J P. Janse van Rensburg, F D Auret, M Diale

Department of Physics, University of Pretoria, Pretoria 0002, South Africa

ARTICLE INFO

Article history:
Received 15 May 2015
Received in revised form
29 July 2015
Accepted 31 July 2015
Available online 1 August 2015

Keywords:
Series resistance
Barrier inhomogeneities
Gaussian distribution & Modified Richardson plot

ABSTRACT

We report on the analysis of current voltage (*I–V*) measurements performed on Pd/ZnO Schottky barrier diodes (SBDs) in the 80–320 K temperature range. Assuming thermionic emission (TE) theory, the forward bias *I–V* characteristics were analysed to extract Pd/ZnO Schottky diode parameters. Comparing Cheung's method in the extraction of the series resistance with Ohm's law, it was observed that at lower temperatures ($T < 180$ K) the series resistance decreased with increasing temperature, the absolute minimum was reached near 180 K and increases linearly with temperature at high temperatures ($T > 200$ K). The barrier height and the ideality factor decreased and increased, respectively, with decrease in temperature, attributed to the existence of barrier height inhomogeneity. Such inhomogeneity was explained based on TE with the assumption of Gaussian distribution of barrier heights with a mean barrier height of 0.99 eV and a standard deviation of 0.02 eV. A mean barrier height of 0.11 eV and Richardson constant value of 37 A cm^{-2} K^{-2} were determined from the modified Richardson plot that considers the Gaussian distribution of barrier heights.

1. Introduction

In realizing semiconductor-based devices, there are various parameters that need to be taken into consideration: surface preparation process, the formation of barrier height between the metal and semiconductor and its homogeneity, density of interface states and dislocations, applied voltage and series resistance (R_s) [1,2]. Amongst all these, the R_s is an important parameter, which causes the electrical characteristics of devices to be non-ideal [3]. There are various techniques to evaluate the main electrical parameters from the forward bias *I–V* measurements such as Cheung and Cheung's method and the Ohm's law [4]. Cheung and Cheung's method brings an alternative approach from Ohm's law to determine the barrier height, ideality factor and R_s from the forward *I–V* measurements, which are the main electrical parameters in the characterisation of a SBDs and provide useful information concerning the nature of the diodes [5].

Analysis of the forward biased *I–V* characteristics of these devices only at room temperature does not give a detailed description about the current conduction mechanism. The investigation of the forward bias *I–V* characteristics in a wide temperature range gives a clear understanding of the aspects of the current transport mechanism and the barrier formation. In general, the forward bias *I–V* characteristics of these devices deviate from the ideal TE theory [6]. There is still some difficulty in predicting the exact transport phenomenon. A careful analysis of the *I–V* characteristics of the SBDs at different temperatures provides detailed information of the conduction process and the nature of the barrier formation at the metal-semiconductor interface [7]. However, in the case of inhomogeneous barrier potential between metal and semiconductor, the structure's barrier potential is resembled to a barrier consisting of higher and lower patches from which current pass through. Thus, it is possible to explain it through TE theory with the Gaussian distribution of the barrier potential [8].

In this study, we analyse temperature dependant forward biased *I–V* measurements on Pd/ZnO SBDs in the 80–320 K temperature range. The series resistance, Schottky Barrier height and ideality factors were calculated using conventional methods as well as alternative methods. Fair correlation is obtained with the alternative methods and the conventional methods in certain areas of the plots. The deviation from ideal TE transport mechanism is been an issue with ZnO materials. Hence, the TE theory with the Gaussian distribution of the barrier potential is used to explain the current transport mechanisms and the determination of the Richardson constant.

2. Experiment

In this study, undoped ZnO samples from Cermet Inc. were

* Corresponding author.
E-mail address: meehleketo@gmail.com (M. Mayimele).

http://dx.doi.org/10.1016/j.physb.2015.07.034
0921-4526/

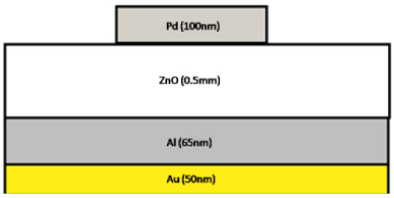

Fig. 1. A schematic diagram of Pd/ZnO SBDs.

used [9]. The samples were degreased in acetone, then methanol for five minutes each in an ultra-sonic bath. They were annealed in nitrogen gas at 800 °C for 30 min and they were again degreased in acetone and methanol. Then etched in 100 °C boiling hydrogen peroxide for three minutes and blown dry with nitrogen gas. Ohmic contacts with composition of Al/Au and relative thicknesses of 65/50 nm were deposited on the Zn polar face using the resistive evaporation technique at a pressure of approximately 1×10^{-6} Torr. Pd Schottky contacts of diameter 0.6 mm and thickness of 100 nm were fabricated on the O-polar face of the ZnO samples using the resistive evaporation system under a vacuum of approximately 1×10^{-6} Torr. Fig. 1 shows the schematic diagram of Pd/ZnO SBDs. Temperature-dependant *I–V* measurements were performed in a closed cycle Helium cryostat in the 80–320 K temperature range.

3. Results and discussion

The current–voltage (*I–V*) characteristics of Pd/ZnO Schottky barrier diodes in the 80–320 K temperature range are plotted in Fig. 2(a). The behaviour of the curves shows strong temperature dependence and a deviation from the ideal Schottky barrier diodes. Assuming standard thermionic emission (TE) theory, the barrier height (Φbo) and ideality factor (n) are extracted using Eqs. (1) and (2) and a linear fit to the *I–V* data [10].

$$\Phi_{bo} = \frac{kT}{q} ln\left[\frac{AA^*T^2}{I_s}\right] \quad (1)$$

and

$$n = \frac{q}{kT}\left(\frac{dV}{dlnI}\right) \quad (2)$$

where I_s is the saturation current, k is the Boltzmann constant, q is the electronic charge, T is temperature in Kelvin, A is the diode area in square centimetres, Φ_{bo} is barrier height in eV and A^* is the Richardson constant, evaluated at 32 A cm^{-2} K^{-2} for n-ZnO [2].

From Eqs. (1) and (2) the values of Φ_{bo} and n of the Pd/ZnO in the 80–320 K temperature range are plotted in Fig. 2(b). The behaviour of the curves show that the Φ_{bo} increases and the n decreases with increasing temperature. This explains the deviation of the *I–V* characteristics from the pure TE mechanism, in which the Φ_{bo} and the n should remain constant with temperature. The higher values of n can be attributed to the presence of barrier height inhomogeneities at the interface, minority carrier injections, the image force effect and the formation of a particular distribution state at the semiconductor band gap [11]. Several researchers [8,12] reported a similar behaviour of the barrier height, which disagree with the negative temperature coefficient of resistance in II–IV metal-semiconductors (MS). Another possible explanation of the observed behaviour is the temperature-activated current transport of charge carriers across the MS interface [13]. At low temperatures, electrons are able to surmount the lower barrier through tunnelling [8]. Therefore, tunnelling will be the dominant transport mechanism of charge carriers through the patches at lower Φ_{bo}. As temperature increase, more electrons access sufficient energy to surmount the barrier height areas through TE, explaining the behaviour of barrier height increasing with increasing temperature [14].

From Fig. 2(a) the forward bias current voltage (*I–V*) characteristics are linear on the semilogarithmic scale from 0.0 V to 0.5 V then deviate due to R_s. Hence, it is of vital importance to determine the R_s using a variety of methods. The simplest way to determine the R_s values is Ohm's law, which yields R_s as dV/dI in the forward bias region and another way of determining the R_s is by Cheung and Cheung's method [1,3]. The forward bias *I–V* characteristics due to TE theory of Schottky diodes with the R_s can be expressed as Cheung's functions [4]:

$$\frac{dV}{d(\ln I)} = IR_s + n\left(\frac{kT}{q}\right) \quad (3)$$

and

$$H(I) = V - n\left(\frac{kT}{q}\right)ln\left(\frac{I}{AA^*T^2}\right) = n\Phi_{bo} + IR_s \quad (4)$$

From Fig. 3(a), the plot is linear with R_s as the gradient and $n\Phi_{bo}$ as the y-axis intercepts derived from Eq. (3). The insert in Fig. 3 (a) shows a plot of the whole range of the forward bias *I–V* data, which can be divided into two regions. In region I, the ideality factor is similar to that obtained using ohm's law, with high values of R_s, where the R_s determined from region II are in good agreement with those of obtained from the *I–V* curves. The observed behaviour can be attributed to the existence of the R_s, interface states and to the voltage drop across the interfacial layers.

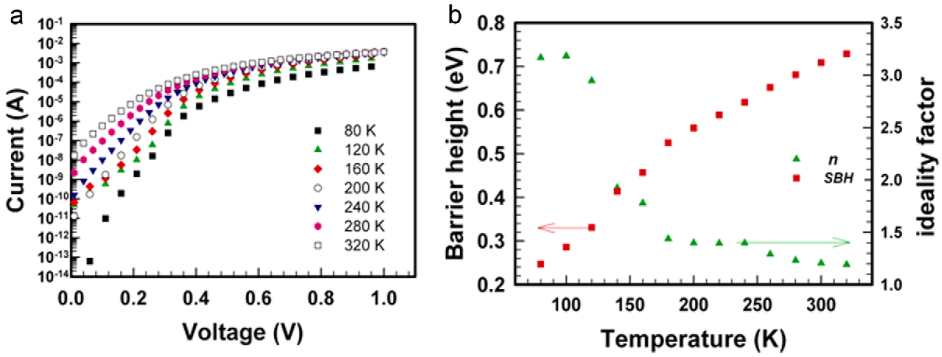

Fig. 2. (a) Semi logarithmic forward current–voltage (*IV*) characteristics, (b) barrier height and ideality factor as a function of temperature for Pd/ZnO SBDs.

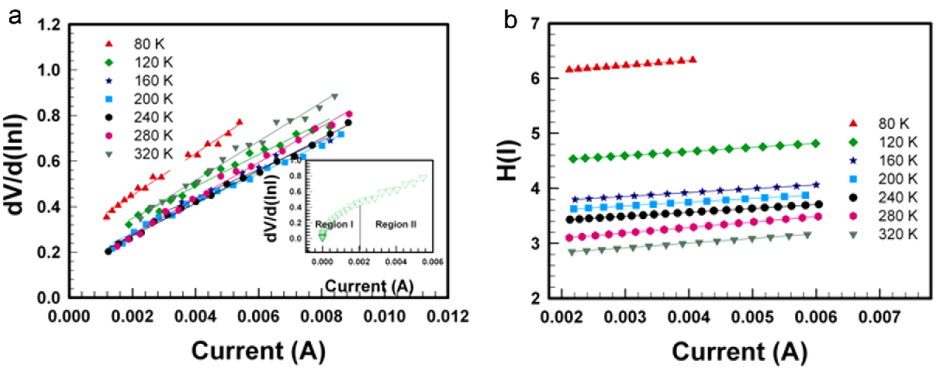

Fig. 3. (a) & (b) Cheung and Cheung's functions against the forward current characteristics of Pd/ZnO SBDs.

Furthermore, the plot of H(I)-I is linear, with the gradient of this plot providing a different determination of R_s. Thus, by using the value of the n obtained from Eq. (3) the value of Φ_{bo} can be calculated from the y-axis intercept of the H(I)-I plot. Similar observations were reported by Durmus et al. [15] on Au/n-Si SBD and Kinaci et al. [5] on Au/TiO2/n-Si SDB.

The R_s obtained from the three different techniques were plotted in Fig. 4(a). Mtangi et al [16] observed a similar trend of series resistance obtained from lnI-V plots on Pd/ZnO SBD in the 60–300 K temperature range. They explained the observed trend to be related to bulk resistivity of the sample determined from the Hall effect measurements, where a transition in the conductivity occurs near 180 K. From Fig. 4(a) shows that at lower temperatures ($T < 180$ K), the R_s decreases with increase in temperatures, while showing an absolute minimum near 180 K and increases linearly with temperature at high temperatures ($T > 200$ K).

As discussed earlier, temperature influences Φ_{bo} (Fig. 2(b)). Another way of determining the Φ_{bo} and the Richardson constant in a range of temperatures, Eq. (1) can be rewritten as,

$$ln\left(\frac{I_s}{T^2}\right) = ln(AA^*) - \frac{q\Phi_{bo}}{kT} \tag{5}$$

Fig. 4(b) shows a plot of the conventional energy variation of ln (I_s/T^2) against $10^3/T$ in the 180-320 K temperature range. Although the entire study of temperature dependant I-V measurements were conducted in the 80–320 K temperature range, a non-linear behaviour was observed at lower temperatures. Hence, linear region of 180–320 K was plotted in Fig. 4(b). The non-linearity of the plot can be attributed to the dependence of the barrier height and the ideality factor on temperature. The Φ_{bo} and Richardson constant were determined from the gradient and the y-axis intercept in Fig. 4(b), respectively. The Richardson constant was determined as 3×10^{-9} A cm^{-2} K^{-2} in the180–320 K temperature range. These values are much lower compared to the theoretical value of 32 A cm^{-2} K^{-2} in n-ZnO. The effective barrier height is 0.26 eV in the 180–320 K temperature range. The deviation in the Richardson plot may be due to the presence of the spatially inhomogeneous barrier height and the potential fluctuations at the interface that consists of low and high barrier areas, i.e. when the temperature is lowered, the current will flow preferentially through the lower barriers in the potential distribution [17–19].

An analytical potential fluctuation method on spatially inhomogeneous SBD can be used to quantitatively explain the non-ideal I–V behaviour of Pd/ZnO Schottky diode, by assuming the Gaussian distribution of the SBH with the mean value of SBH $(\overline{\Phi}_{bo}(T=0))$ and a standard deviation (σ_{so}) of the SBH distribution. The total current in a given forward bias V is then given by

$$I = I_s \exp\left(\frac{qV}{n_{ap}kT}\right)\left[1 - exp\left(\frac{-qV}{kT}\right)\right] \tag{6}$$

with

$$I_s = AA^*T^2 \exp\left(\frac{q\Phi_{ap}}{kT}\right), \tag{7}$$

Where n_{ap} and Φ_{ap} are the apparent ideality factor and apparent Schottky barrier height, respectively, given by [17]

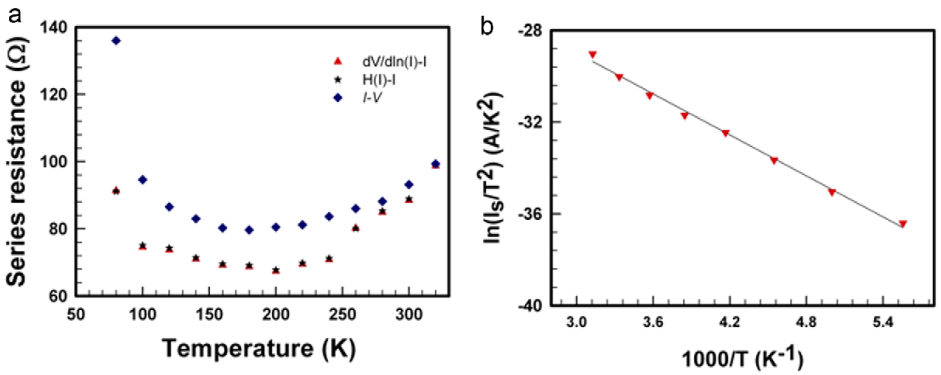

Fig. 4. (a) Series resistance as a function of temperature using 3 different methods and (b) Richardson plot, $ln\ (I_s/T^2)$ versus 1000/T for Pd/ZnO SBDs.

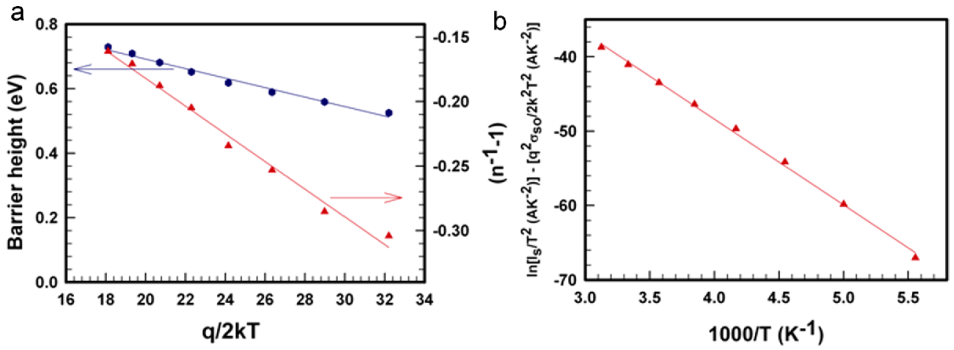

Fig. 5. (a) Zero-bias apparent barrier height and the inverse ideality factor versus *q/2kT* and (b) Modified Richardson plot for the Pd/ZnO SBDs according to the Gaussian distribution of the barrier heights.

$$\Phi_{ap} = \overline{\Phi}_{bo}(T=0) - \frac{q\sigma_{so}^2}{2kT} \tag{8}$$

$$\left(\frac{1}{n_{ap}} - 1\right) = -\rho_2 + \frac{q\rho_3}{2kT} \tag{9}$$

Here ρ_2 and ρ_3 are voltage coefficients, which may depend on temperature, used to quantify the voltage deformation of the SBH distribution [20]. Fig. 5(a) shows a linear plot of barrier height vs. $q/2kT$, ($\overline{\Phi}_{bo}(T=0)$) and σ_{so}, which were extracted using Eq. (8) as the *y*-axis intercept and the gradient obtained as 0.99 eV and 0.02 V, respectively. The smaller the value of the σ_{so}, the more homogeneous the barrier height is and the better the diode. A linear plot of ideality factor vs. $q/2kT$, using Eq. (9) shown in Fig. 4 (a) gives the voltage coefficients ρ_2 and ρ_3 as the intercepts and gradient, respectively, are obtained as 0.03 and −0.01 eV, respectively. The linear behaviour of the plot shows that the ideality factor expresses the voltage deformation of the Gaussian distribution of the SBD.

The Richardson constant extracted from the conventional activation energy $ln(I_s/T^2)$ vs. $1000/T$ plot was much lower than the theoretical value due to the lateral inhomogeneity of the Schottky barrier. A more reliable value of the Richardson constant can be determined using modified Arrhenius plot by eliminating the effect of the inhomogeneity. A modified expression according to the Gaussian distribution of the SBHs can be obtained by using Eqs. (8) and (9) in Eq. (5) as

$$\ln\left(\frac{I_s}{T^2}\right) - \left(\frac{q^2\sigma_o^2}{2k^2T^2}\right) = ln(AA^{**}) - \left[\frac{q\Phi_{bo}}{kT}\right] \tag{10}$$

The modified $ln(I_s/T^2) - (q^2\sigma_o^2)/(2k^2T^2)$ vs. 1000/T plot shown in Fig. 5(b) should yield a straight line following the Eq. (10) with the gradient directly yielding the mean Φ_{bo} and the intercept at the y-axis yielding the modified Richardson constant (A^{**}). The values of $ln(I_s/T^2) - (q^2\sigma_o^2)/(2k^2T^2)$ were calculated using the value of σ_{so}. From the plot, the mean Φ_{bo} and A^{**} were determined to be 0.99 eV and 37 A cm^{-2} K^{-2} without using the temperature coefficients of the barrier heights, respectively. The mean Φ_{bo} extracted using the modified Richardson plot was identical to 0.99 eV obtained from the plot of barrier height vs. $q/2kT$ as shown in Fig. 5(a). Furthermore, the modified Richardson constant of 37 A cm^{-2} K^{-2} is very close to the theoretical value of n-ZnO of 32 A cm^{-2} K^{-2}, implying the validity of the analytical model predicting the Gaussian type of the barrier height distribution in Pd/ZnO Schottky diode.

4. Conclusion

Analysis of the forward bias *I–V* measurements of Pd/ZnO Schottky barrier diodes were investigated in a wide temperature range of 80–320 K. The series resistance obtained in this study are in good agreement with literature and with each other. The current transport mechanism at lower temperature is dominated by the current flow through the low Schottky barrier areas and tunnelling. Meanwhile at high temperatures, TE is the dominant current transport mechanism. Barrier height and the ideality factor decreased and increased, respectively, with decreasing temperature, attributed to the existence of barrier height inhomogeneity. Such inhomogeneity has been successfully explained based on TE with the assumption of Gaussian distribution of barrier heights with a mean barrier height of 0.986 eV and a standard deviation of 0.015 V. A mean barrier height of 0.994 eV and Richardson constant value of 37 A cm^{-2} K^{-2} were determined from the modified Richardson plot that considers the Gaussian distribution of barrier heights.

Acknowledgement

The South Africa National Research Foundation (NRF) and the University of Pretoria for financial support.

References

[1] F.Z. Pür, A. Tataroğlu, Phys. Scr. 86 (2012) 035802.
[2] Ü. Özgür, Y.I. Alivov, C. Liu, A. Teke, M.A. Reshchikov, S. Doğan, V. Avrutin, S.-J. Cho, H. Morkoç, J. Appl. Phys. 98 (2005) 041301–041301-103.
[3] Z. Ahmad, M.H. Sayyad, Physica E 41 (2009) 631–634.
[4] S.K. Cheung, N.W. Cheung, Appl. Phys. Lett. 49 (1986) 85–87.
[5] B. Kinaci, T. Asar, Y. Özen, S. Özçelik, Optoelectron. Adv. Mater. Rapid Commun. 5 (2011) 434–437.
[6] E. Gür, S. Tüzemen, B. Kiliç, C. Coşkun, J. Phys. Condens. Matter (2007) 196–206.
[7] J.-Y. Jeong, V. Janardhanam, H.-J. Yun, J.-H. Lee, J.-Y. Kim, K.-H. Shim, C.-J. Choi, Jap. J. Appl. Phys. 53 (2014) 08NH01.
[8] H. Tecimer, A. Türüt, H. Uslu, Ş. Altındal, İ. Uslu, Sens. Actuators A: Phys. 199 (2013) 194–201.
[9] http://www.cermetinc.com/materials/n__ZnO_substrate_product_lit.2014.
[10] S. Sze, K.K. Ng, Physics of Semiconductor Devices: Third Edition, 2006.
[11] D. Korucu, T.S. Mammadov, J. Optoelectron. Adv. Mater. 14 (2012) 41–48.
[12] B.G. Yacobi, Semiconductor Materials, An Introduction to Basic Principles, Springer, US, 2013.
[13] M.A. Mayimele, M. Diale, W. Mtangi, F.D. Auret, Mater. Sci. Semicond. Process. 34 (2015) 359–364.
[14] I. Hussain, M. Soomro, N. Bano, O. Nur, M. Willander, J. Appl. Phys. 113 (2013) 234509.
[15] P. Durmuş, M. Yıldırım, Mater. Sci. Semicond. Process. 27 (2014) 145–149.

[16] W. Mtangi, Electrical Characterization of ZnO and Metal ZnO Contacts, University of Pretoria, South Africa, 2009.
[17] A. Özdemir, A. Turut, A. Kökçe, Semicond. Sci. Technol. 21 (2006) 298.
[18] S.M. Faraz, V. Khranovskyy, R. Yakimova, A. Ulyashin, Q. Wahab, IEEE Regional Symposium on Micro and Nanoelectronics (RSM), 2011, 48–51.
[19] H. Asil, K. Çinar, E. Gür, C. Coşkun, S. Tüzemen, Int. J. 8 (2013) 371–379.
[20] E. Özavcı, S. Demirezen, U. Aydemir, Ş. Altindal, Sens. Actuators A Phys. 194 (2013) 259–268.

Reference

[1] A.B. Djurišić, A.M.C. Ng, X.Y. Chen, Progress in Quantum Electronics, **34** (2010) 191.

[2] S.K. Arya, S. Saha, J.E. Ramirez-Vick, V. Gupta, S. Bhansali, S.P. Singh, Analytica Chimica Acta, **737** (2012) 1.

[3] A. Janotti, C.G. Van de Walle, Physical Review B, **76** (2007) 165202.

[4] M. McCluskey, S. Jokela, Physica B: Condensed Matter, **401** (2007) 355.

[5] Ü. Özgür, Y.I. Alivov, C. Liu, A. Teke, M.A. Reshchikov, S. Doğan, V. Avrutin, S.-J. Cho, H. Morkoç, Journal of Applied Physics, **98** (2005) 14025.

[6] A. Janotti, C.G. Van de Walle, Reports on Progress in Physics, **72** (2009) 126501.

[7] S.J. Pearton, D.P. Norton, K. Ip, Y.W. Heo, T. Steiner, Progress in Materials Science, **50** (2005) 293.

[8] H. Morkoç, U. Özgür, Zinc Oxide: Fundamentals, Materials and Device Technology, (2009).

[9] M.W. Allen, S.M. Durbin, Applied Physics Letters, **92** (2008)103520.

[10] A.R. Peaker, V.P. Markevich, I.D. Hawkins, B. Hamilton, K. Bonde Nielsen, K. Gościński, Physica B: Condensed Matter, **407** (2012) 3026.

[11] L. Dobaczewski, P. Kaczor, M. Missous, A. Peaker, Z. Żytkiewicz, Physical review letters, **68** (1992) 2508.

[12] O. Schmidt, P. Kiesel, C.G. Van de Walle, N.M. Johnson, J. Nause, G.H. Döhler, Japanese Journal of Applied Physics, **44** (2005) 7271.

[13] D.V. Lang, Journal of Applied Physics, **45** (1974) 3023.

[14] M.A. Mayimele, M. Diale, W. Mtangi, F.D. Auret, Materials Science in Semiconductor Processing, **34** (2015) 359.

[15] S.S. Naik, V.R. Reddy, Advanced Materials Letters, **3** (2012) 188.

[16] D.S. Reddy, M.B. Reddy, N.N.K. Reddy, V.R. Reddy, Journal of Modern Physics, **2** (2011) 113.

[17] D.C. Look, Materials Science and Engineering: B, **80** (2001) 383.

[18] W. Körner, C. Elsässer, Physical Review B, **81** (2010) 085324.

[19] H. Heinrich, ZAMM - Journal of Applied Mathematics and Mechanics **49** (1969) 571.

[20] W. Fan, A. Abiyasa, S. Tan, S. Yu, X. Sun, J. Xia, Y. Yeo, M. Li, T. Chong, Journal of crystal growth, **287** (2006) 28.

[21] J.J. Quinn, K.S. Yi, Solid state physics: Principles and modern applications (2009).

[22] A.F. Kohan, G. Ceder, D. Morgan, C.G. Van de Walle, Physical Review B, **61** (2000) 15019.

[23] P.J. Kelly, R.D. Arnell, Vacuum, **56** (2000) 159.

[24] H.-U. Krebs, M. Weisheit, J. Faupel, E. Süske, T. Scharf, C. Fuhse, M. Störmer, K. Sturm, M. Seibt, H. Kijewski, D. Nelke, E. Panchenko, M. Buback, Pulsed Laser Deposition (PLD) -- A Versatile Thin Film Technique, in: B. Kramer (Ed.) Advances in Solid State Physics, Springer Berlin Heidelberg (2003) 505.

[25] J.R. Arthur, Surface Science, **500** (2002) 189.

[26] C.R. Gorla, N.W. Emanetoglu, S. Liang, W.E. Mayo, Y. Lu, M. Wraback, H. Shen, Journal of Applied Physics, **85** (1999) 2595.

[27] A.C. Jones, Journal of Crystal Growth, **129** (1993) 728.

[28] Z. Ahmad, M.H. Sayyad, Physica E: Low-dimensional Systems and Nanostructures, **41** (2009) 631.

[29] M. Shiloh, J. Gutman, Journal of Crystal Growth, **11** (1971) 105.

[30] R.A. Laudise, E.D. Kolb, A.J. Caporaso, Journal of the American Ceramic Society, **47** (1964) 9-12.

[31] Y. Liu, J. Ma, F. Liu, Y. Zang, Y. Liu, Journal of Semiconductors, **35** (2014) 12924.

[32] G.H. Kassier, M. Hayes, F.D. Auret, M. Mamor, K. Bouziane, Journal of Applied Physics, **102** (2007) 014903.

[33] F.D. Auret, S.A. Goodman, M.J. Legodi, W.E. Meyer, D.C. Look, Applied Physics Letters, **80** (2002) 1340.

[34] E.V. Lavrov, F. Börrnert, J. Weber, Physical Review B, **71** (2005) 035205.

[35] F.D Auret, A.W.R Leitch, J.S Vermaak, S. Afr. J. Phys. **59** (1986) 158.

[36] G. Xing, Y. Lu, Y. Tian, J. Yi, C. Lim, Y. Li, G. Li, D. Wang, B. Yao, J. Ding, AIP Adv, **1** (2011) 022.

[37] J.L. Lyons, A. Janotti, C.G. Van de Walle, Applied Physics Letters, **95** (2009) 252105.

[38] C.G. Van de Walle, Physical Review Letters, **85** (2000) 1012.

[39] W. Mtangi, F.D. Auret, M. Diale, W.E. Meyer, A. Chawanda, H. De Meyer, P. Janse van Rensburg, J.M. Nel, Journal of Applied Physics, **11**1 (2012) 084503.

[40] E.H. Rhoderick, IEE Proceedings I: Solid State and Electron Devices, **129** (1982) 1.

[41] E.H. Rhoderick, Journal of Physics D: Applied Physics, **3** (1970) 1153.

[42] S. Sze, K.K. Ng, Physics of Semiconductor Devices: Third Edition, 2006.

[43] R.H. Rhoderick, R.H Williams, Metal-semiconductor contacts, Clarendon Press ; Oxford University Press, Oxford[England]; New York, 1988.

[44] S.K Benerjee. B.G. Streetman, Solid State Electronic Devices, 6th Edition, (2005).

[45] R. Tung, Physical Review B, **45** (1992) 1350.

[46] J. Sólyom, Fundamentals of the physics of solids **2** (2009).

[47] R. Williams, Journal of Vacuum Science and Technology, **18** (1981) 929.

[48] S.M. Faraz, V. Khranovskyy, R. Yakimova, A. Ulyashin, Q. Wahab, RSM2011, Kota Kinabalu, Malaysia, (2011) 58.

[49] E. Gür, S. Tüzemen, B. Kiliç, C. Coşkun, Journal of Physics: Condensed Matter, 2007, pp. 196206.

[50] H.L. Mosbacker, Y.M. Strzhemechny, B.D. White, P.E. Smith, D.C. Look, D.C. Reynolds, C.W. Litton, L.J. Brillson, Applied Physics Letters, **87** (2005) 012102.

[51] J.H. Werner, H.H. Güttler, Journal of Applied Physics, **69** (1991) 1522.

[52] Y. Song, R. Van Meirhaeghe, W. Laflere, F. Cardon, Solid-state electronics, **29** (1986) 633.

[53] İ. Dökme, Ş. Altindal, M.M. Bülbül, Applied Surface Science, **252** (2006) 7749.

[54] S. Chand, Semiconductor Science and Technology, **19** (2004) 82.

[55] A. Gümüş, A. Türüt, N. Yalçin, Journal of Applied Physics, **91** (2002) 245.

[56] W. Mtangi, F.D. Auret, C. Nyamhere, P.J. Janse van Rensburg, C.M.D. A, Physica B: Condensed Matter, **404** (2009) 1092.

[57] M.A. Mayimele, J.P.J. van Rensburg, F.D. Auret, M. Diale, Physica B: Condensed Matter 480 (2015) 58.

[58] P.N.K Deenapanray, F.D Auret, Critical Reviews in Solid State and Materials Sciences, **29** (2004) 1.

[59] Y. Zohta, M.O. Watanabe, Journal of Applied Physics, **53** (1982) 1809.

[60] J.-Y. Jeong, V. Janardhanam, H.-J. Yun, J.-H. Lee, J.-Y. Kim, K.-H. Shim, C.-J. Choi, Japanese Journal of Applied Physics, **53** (2014) 08NH01.

[61] F.Z. Pür, A. Tataroğlu, Physica Scripta, **86** (2012) 035802.

[62] H. Zhang, E.J. Miller, E.T. Yu, Journal of Applied Physics, **99** (2006) 023703.

[63] İ. Taşçıoğlu, U. Aydemir, Ş. Altındal, B. Kınacı, S. Özçelik, Journal of Applied Physics, **109** (2011) 10221.

[64] S.K. Cheung, N.W. Cheung, Applied Physics Letters, **49** (1986) 85.

[65] P. Durmuş, M. Yıldırım, Materials Science in Semiconductor Processing, **27** (2014) 145.

[66] B. Kinaci, T. Asar, Y. Özen, S. Özçelik, Optoelectronics and Advanced Materials, Rapid Communications, **5** (2011) 434.

[67] W. Mtangi, F.D. Auret, P. Janse van Rensburg, S. Coelho, M.J. Legodi, J. Nel, W. Meyer, A. Chawanda, Journal of Applied Physics, **110** (2011) 094504.